Revealing the Structural Coloration of Self-Assembled Chitin Nanocrystal Films

*Aurimas Narkevicius, Richard M. Parker, Jordi Ferrer-Orri, Thomas G. Parton, Zihao Lu, Gea T. van de Kerkhof, Bruno Frka-Petesic, and Silvia Vignolini**

Dr. Aurimas Narkevicius, Dr. Richard M. Parker, Jordi Ferrer-Orri, Thomas G. Parton, Zihao Lu, Dr. Gea T. van de Kerkhof, Dr. Bruno Frka-Petesic, Prof. Silvia Vignolini
Yusuf Hamied Department of Chemistry, University of Cambridge, Lensfield Road, Cambridge, CB2 1EW, United Kingdom.

E-mail: sv319@cam.ac.uk

Keywords: chitin, nanocrystals, self-assembly, structural color, liquid crystals

Abstract

The structural coloration of arthropods often arises from helicoidal structures made primarily of chitin. Although it is possible to achieve analogous helicoidal architectures by exploiting the self-assembly of chitin nanocrystals (ChNCs), to date no evidence of structural coloration has been reported from such structures. In this work, we identify that previous studies were constrained by both the experimental inability to access sub-micron helicoidal pitches and the intrinsically low birefringence of crystalline chitin. To expand the range of accessible pitches, here we isolate ChNCs from two phylogenetically distinct sources of α-chitin, namely fungi and shrimp, while to increase the birefringence, we perform an *in situ* alkaline treatment, increasing the intensity of the reflected color by nearly two orders of magnitude. By combining this treatment with precise control over suspension formulation, we demonstrate structurally colored chitin-based films with reflection tunable from blue to near infrared.

1 Introduction

To meet the growing demand for functional materials with tailored properties, the pursuit of optimal performance must be balanced against a consideration of the sustainability of the source materials.[1,2] One approach to address this challenge is to take inspiration from the natural world, where a limited selection of simple components can be assembled into various hierarchical structures to achieve diverse functionalities.[3] This concept is well exemplified in arthropods, such as insects, spiders and crustaceans, where numerous structural functions are achieved using chitin as the primary building block.[4] The chains of this polysaccharide are assembled into fibrillar units, which are tightly bound together by a dense network of hydrogen bonds and van der Waals interactions.[5] These microscale fibrils then form the building blocks for larger-scale architectures. In particular, the arrangement of fibrils into a helicoidal configuration, where they are locally aligned with a twist perpendicular to the alignment axis, is a ubiquitous motif across the *Arthropoda* phylum.[6] Notable examples are the dactyl clubs of the mantis shrimp,[7] which incorporates a helicoidal architecture with large, micron-scale periodicity (termed 'pitch') responsible for reducing crack propagation, or the cuticle of the scarab beetle,[8] whose striking structural coloration arises from a helicoidal nanostructure with a pitch on the length-scale of visible light (i.e. 250 – 450 nm).[9,10] However, despite being an abundant, biodegradable and versatile biomaterial, the potential of chitin as a feedstock for bespoke optical materials has not yet been realized.[11,12]

Helicoidal nano-architectures can be reproduced by exploiting the self-assembly of chitin nanocrystals (ChNCs), which are elongated nanoparticles obtained by the acid hydrolysis of purified natural chitin.[13–15] In acidic aqueous media, ChNCs spontaneously self-organize into a chiral nematic (*i.e*, cholesteric) liquid crystalline phase.[14–17] The chiral ordering of this mesophase can be preserved as the suspension dries into the solid state.[14,15,18] This self-assembly process is tunable through both the properties of the ChNCs (e.g. surface charge, morphology, size) and the formulation of the medium (e.g. ionic strength, pH).[15,16] However, structural coloration in the visible range has not yet been reported for artificial chitin architectures[11] because the smallest pitches reported so far are ~ 650 nm.[15]

In this work, we demonstrate structural coloration in ChNC films by overcoming previous limitations in pitch and birefringence. To do so, we compare ChNCs extracted from two phylogenetically distinct sources of α-chitin, namely from fungi (f-ChNCs) and shrimp (s-ChNCs). We observed that helicoidal f-ChNC films can access the pitch range required for reflection across the visible spectrum. We then enhance the intrinsic birefringence within the helicoidal structure by employing an *in situ* alkaline treatment to convert chitin into chitosan, increasing the intensity of the reflected color by nearly two orders of magnitude. By combining this treatment with careful control over the formulation, we demonstrate photonic films that reflect red color when using s-ChNCs, and blue, green, and red colors when using f-ChNCs.

2 Results and Discussion

2.1 Self-assembly of ChNCs into helicoidal films

Fungal chitin was extracted from a fresh sample of the common mushroom *Agaricus bisporus*, while shrimp chitin was refined from commercial shrimp chitin powder (Fisher Scientific, practical grade). A series of similar purification steps were performed to obtain pure α-chitin from each source (see Experimental Methods), with the purification process monitored by ^{13}C ss-NMR spectroscopy, p-XRD, and ATR-FTIR spectroscopy (**Figure S1-S3**). To produce ChNCs, the purified chitin was then subjected to hydrolysis with hydrochloric acid (3.0 M, 60 mL/g_{chitin}, 100 °C). Fungal chitin was hydrolyzed for 180 minutes as a longer duration resulted in significant discoloration, indicating the occurrence of undesirable side-reactions, whereas shrimp chitin was carried out for 270 minutes (previously reported to be the optimal conditions[15]). The resultant f-ChNC and s-ChNC suspensions were diluted to 1.0 wt% and dialyzed against a hydrochloric acid solution ([HCl] = 0.6 mM) until the conductivity of the dialysis bath was constant. The suspensions were then ultrasonicated, resulting in colloidally stable suspensions ([ChNC] = 1.0 wt%).

The self-assembly of f-ChNCs and s-ChNCs was first investigated by preparing suspensions at a range of ChNC concentrations and observing their equilibrium phase behavior in glass capillaries. This revealed that while both suspensions could form a chiral nematic phase, their properties were significantly different (**Figure 1B, S4**). Although both suspensions were isotropic at a ChNC concentration of 1.0 wt%, the f-ChNC suspension showed biphasic behavior (indicating liquid crystal ordering) from 1.75 wt%, compared to 3.0 wt% for the s-ChNC suspension. A consequence of this earlier transition was that the f-ChNC suspension formed a fully anisotropic chiral nematic phase at 4.5 wt%, while the s-ChNC remained predominantly isotropic, with a fully anisotropic phase not reached till 9.0 wt%. The earlier onset of the chiral nematic phase in f-ChNCs is consistent with their larger mean aspect ratio (as determined by TEM and AFM, **Figure S5**), in accordance with Onsager's theory for lyotropic liquid crystals.[19] Moreover, the chiral nematic phase of a f-ChNC suspension had a significantly smaller pitch than an s-ChNC suspension at comparable concentration, ionic strength and pH, indicating a stronger chiral interaction between f-ChNCs.[15,16] While the origin of a chiral mesophase in ChNCs suspensions is not well understood, recent studies on cellulose nanocrystals, a similar colloidal system, have demonstrated that the presence of crystallite bundles determines the chiral nematic pitch.[20,21] Qualitative observation of TEM images confirmed the presence of crystallite bundles (**Figure S5**), but further quantitative analysis is required to confirm whether these bundles are also the origin of mesophase chirality in ChNC suspensions.

ChNC photonic films were prepared by slow evaporation of aqueous suspensions of f-ChNCs and s-ChNCs. In both cases, cross-sectional SEM revealed the characteristic Bouligand arches expected for a helicoidal structure,[22] with the pitch (p) measured as 360 ± 90 nm for f-ChNCs (**Figure 1C, S6C**) and 4.0 ± 1.9 μm for s-ChNCs (**Figure S6B**). The peak reflection wavelength of a helicoidal structure at normal incidence is given by Bragg's law ($\lambda = n_{\mathrm{avg}}\, p$), where n_{avg} is the mean refractive index reported to be approximately 1.55 for chitin.[11,23,24] It is therefore expected that the pitch of the f-ChNC film is in the range to reflect visible color, while the pitch of the s-ChNC film is too large.[14,15] While both films appeared macroscopically transparent (e.g. **Figure 1C inset**), very weak coloration could be observed

using polarized microscopy on f-ChNC films (**Figure 1D**). When imaged between crossed linear polarizers in epi-illumination, green and red regions could be observed. The former are consistent with the minimum pitch measured by SEM, while the latter are attributed to tilted domains that experience less axial compression upon drying and have a larger final pitch, as previously been described for analogous structures.[25,26] An example SEM cross-section showing tilted domains within a ChNC film is reported in **Figure S14D**. A green region in the f-ChNC film was characterized by micro-spectroscopy between crossed polarizers (**Figure 1E**, see Experimental Methods), which revealed a narrow reflection peak with very low reflectance (< 1%) that is consistent with the lack of visible macroscopic coloration.

2.2 Tuning the helicoidal pitch of photonic ChNC films

The pitch of ChNC films can be tuned by varying the ionic strength and pH of the cast suspension (**Figure 2A, 2B**).[15] To explore this concept, the f-ChNC suspension was extensively re-dialyzed against Milli-Q water. During this process the ionic strength of the suspension became extremely low and the pH tended to neutrality, leaving only a fraction of the surface amines protonated (pK_a = 6.3).[14] Sodium chloride (NaCl) can then be added to increase the ionic strength without changing the level of protonation. Alternatively, addition of hydrochloric acid (HCl) first increases the degree of protonation of the surface-bound amines. Once the surface is fully protonated, further addition of HCl simply contributes to the ionic strength, analogous to the effect of adding NaCl. The amount of HCl required to fully protonate an f-ChNC suspension (expressed as moles of ions per ChNC dry mass) was determined to be 246 mmol/kg by conductometric titration (**Figure S7**), consistent with the observed significant decrease in viscosity of the f-ChNC suspension above 250 mmol/kg of added HCl. As the surface-bound amines become protonated, the overall charge of the nanoparticles increases, which was found to red-shift the reflected color of the resultant f-ChNC films (**Figure 2A**). Once all the surface amines are protonated (i.e. [HCl] > 246 mmol/kg), addition of further monovalent electrolyte (HCl or NaCl) results in a subsequent blue-shift in the color of the f-ChNC film (**Figure 2B**), followed by a reversal towards red wavelengths beyond 150 mmol/kg of additional electrolyte. By controlling the initial formulation of the f-ChNC suspension in

terms of the amounts of HCl and/or NaCl added, f-ChNC films that reflect wavelengths ranging from 550 nm (green) to 1000 nm (infrared) could be obtained. Similarly, by controlling the initial formulation of the s-ChNC suspension, the pitch could be reduced to the smallest value of 648 ± 77 nm, still too large for visible structural coloration (**Figure S8A-C, S9E, F**). Micro-spectroscopy in the infrared region of the s-ChNC films confirmed reflection peaks at various wavelengths above 850 nm arising from domains with different pitch and orientation. (**Figure S8G**). While the values of pitch in the s-ChNC and f-ChNC films are clearly different, the intensities of the reflection peaks are of the same order of magnitude, suggesting that their local optical properties (e.g. birefringence, alignment) are broadly consistent.

2.3 Elucidating the optical properties of photonic ChNC films

The weak reflectance of the ChNC films can be explained by considering the birefringence of chitin and the dimensions of individual domains. By modeling a left-handed helicoidal structure as a stack of birefringent layers with a fixed rotation angle between each layer, it can be shown that for structures with small birefringence relative to the average refractive index ($\Delta n \ll n_{\text{avg}}$) the peak reflectance of left-circularly polarized (LCP) light at normal incidence is given by

$$R_{LCP} = \tanh^2\left(\pi\, \Delta n\, t / n_{\text{avg}}\, p\right) \qquad \text{(Eq. 1)}$$

where t is the domain thickness and p is the pitch (see Supporting Information for extended derivation based on the work of de Vries).[23] This equation shows the importance of birefringence for achieving high LCP reflectance, as illustrated by **Figure 3F**.

Experimentally, the LCP reflectance of the chiral nematic structure is hard to distinguish from the broadband specular reflection at the film-air interface due to its low intensity. We therefore measured the reflectance of the film in crossed polarizer configuration, R_{XP}, (**Figure 1E**) to isolate the contribution from the helicoidal structure. To compare this theoretical prediction to experimental values, the ChNC domain thickness was first estimated by cross-sectional SEM, which indicated t/p values up to 40 (**Figure S14**). The reflectance of f-ChNC films was then measured by micro-spectroscopy and found to have a maximum

value of R_{XP} = 0.0036 (**Figure S15A**). Using Eq. 1 and assuming the brightest reflection comes from the largest domains, these values suggest an extremely small effective birefringence of ChNCs of $\Delta n \approx$ 0.0007–0.0015 (indicated by the red shaded area in **Figure 3F**), consistent with previous estimates of the birefringence of α-chitin in natural and synthetic structures.[8,27] For context, cellulose nanocrystals (CNCs), which are known to produce intense structural coloration from analogous helicoidal films, have a much higher effective and intrinsic birefringence ($\Delta n_{\mathrm{CNC\,eff}} = 0.062$ and $\Delta n_{\mathrm{CNC}} = 0.081$, respectively).[28–30] The difference between the two values is related to the local alignment of individual nanocrystals within the helicoidal structure (see Supporting Discussion S2).[31] As indicated by the gray shaded area in **Figure 3F,** the much greater birefringence of photonic CNC films leads to near-saturated reflection for $t/p > 10$. To attain a comparable reflectance (e.g. $R_{LCP} > 0.9$) from a ChNC film with a pitch of 400 nm and assuming the upper limit of our birefringence range, the thickness of a single uniform domain would still need to exceed 240 μm (i.e., $t/p > 600$), which is experimentally near-impossible to achieve. In addition, while the imaginary refractive index of chitin is small (ca. 3.0×10^{-4})[32] and thus absorption can be neglected for the films studied in this work (i.e. 20 – 40 μm thick), it is expected that absorption would become significant for films in this thickness range (i.e. >240 μm). These findings highlight the importance of increasing the birefringence of the nano-rods, rather than aiming for thicker monodomain films, to significantly increase the film reflectance.

2.4 *In situ* conversion of chitin to chitosan

It is well established that exposure of cleaned crab and shrimp shells to strong base at elevated temperatures produces structural color.[11,33,34] This artificial treatment not only removes protein from the chitinaceous cuticles, but also can convert chitin into its derivative, chitosan (**Figure S10**). Given the broad and strong reflectance peaks achieved by this method, we postulate that the enhancement of the visual appearance must arise from an increase in the intrinsic birefringence. With this in mind, to enhance the birefringence of our ChNC films, we applied an alkali treatment (50 wt% NaOH, 90 ºC, 8 h), to

successfully concert chitin into chitosan, verified by ATR-FTIR spectroscopy (**Figure S11**).[35] When imaged by polarized optical microscopy, fragments of an f-ChNC film with and without alkaline treatment reveal a dramatic 50-fold enhancement in the reflected intensity and a substantial blue-shift in reflected color, as exemplified in **Figure 3A-E, S15**. The decrease in pitch correlates with the 10-20% reduction in film thickness (**Figure S9**) and is attributed to the removal and solubilization of the acetyl groups, which represent *ca*. 20 % of the molecular weight of chitin. Therefore, assuming that the helicoidal domain distribution (*i.e.* t/p) has not changed, as the material retains the shape throughout the treatment, the only explanation for this significant increase in coloration is an increase in intrinsic birefringence upon conversion from chitin to chitosan. Considering the 50-fold increase of reflectance ($R_{XP} \approx 0.175$) and assuming no substantial change of the average refractive index of the films, we estimate from **Eq. 1** the effective birefringence of the chitosan-converted films as $\Delta n_{\mathrm{deAc}} \approx 0.005–0.015$, i.e. an order of magnitude increase. From this estimation, the minimum domain thickness to approach saturating reflection ($R_{LCP} > 0.9$) is only 20 µm (i.e., $t/p \approx 60$), which is comparable to the largest domains observed in our SEM analysis. Finally, the prominence of the LCP peak reflectance reported in **Figure S12E** ($R_{LCP} \approx 0.3$) is consistent with this estimation, as a domain thickness of $t/p \approx 40$ predicts a birefringence of $\Delta n_{\mathrm{deAc}} \approx 0.008$ (see blue shaded area in **Figure 3F**).

The combination of f-ChNC self-assembly and alkaline post-treatment was then exploited to produce structurally colored films across the visible spectrum (**Figure 4**). The alkaline treatment has the dual effect of reducing the helicoidal pitch and increasing birefringence, so a weakly-colored green film (**Figure 1D**) becomes a vivid blue film after treatment (**Figure 4A**). Green and red f-ChNC photonic films can analogously be produced by tuning the formulation of the initial suspension (**Figure 4B, C,** see Experimental Methods). The stronger reflectance of the post-treatment films was confirmed by reflection micro-spectroscopy (**Figure 4D**), and their color purity visualized using a CIE 1931 chromaticity diagram (inset in **Figure 4D**). For the s-ChNC films the significant reduction in pitch upon conversion from chitin to chitosan is crucial for visible coloration, with the initially weak infrared film displaying a strong red

coloration after treatment (**Figure S8, S9E-H**). Furthermore, while the colored films are stable under ambient conditions, they are both biodegradable and readily dissolved in weakly acidic conditions, enabling the recycling of this material for other uses, e.g. fertilizer.[36] Ultimately, the ability to tune colors from blue to infrared exemplifies the potential of ChNCs for sustainable photonic materials.

2.5 Comparison with natural chitinaceous helicoidal structures

Beyond the self-assembly of photonic films from ChNCs, these studies offer some insight into their naturally occurring analogues. Numerous species of beetle employ chitinaceous helicoidal structures in their cuticles to produce brilliant structural color. It is perhaps surprising, therefore, that the untreated ChNC films in this work exhibit only a faint optical response, indicating that the intrinsic birefringence of α-chitin alone is insufficient to explain the vibrant coloration observed from natural structures. Insect cuticles contain only approx. 30% of chitin by composition, with the remainder being mostly made up by proteins, which suggests that the overall birefringence must be enhanced by the distribution of these other chemical components.[6] Attempts here to replicate this effect via the addition of poly(ethylene glycol) into the ChNC film (**Figure S16**) did not significantly increase the intensity of the reflected color, which could be attributed to the small refractive index contrast ($\Delta n < 0.1$) and/or insufficient amount of additive (limited to less than 20 wt% to remain in visible regime). Alternatively, the intense reflection observed in some beetle species (e.g., *Plusiotis resplendens* or *Plusiotis optima*) relies on the incorporation of highly birefringent uric acid within the helicoidal structure,[8] suggesting that the chitin nanostructure mainly acts as a template in these species. In contrast, the conversion of chitin into chitosan employed in this work is unlikely to explain the optical response of natural helicoidal structures, as chitosan is not typically found in the arthropod cuticle in significant quantities.

3 Conclusions

Structurally colored chitin nanocrystal films with tunable color across the visible spectrum were successfully fabricated using fungal ChNCs. The distinctive mesophase behavior of f-ChNCs gave access

to much smaller helicoidal pitches in the solid-state when compared to shrimp ChNCs. The very low reflectance of the pristine ChNC films ($\lesssim 1\%$) was overcome by an alkaline post-treatment, which converts chitin to chitosan, causing both a blue-shift in the reflected wavelength (10 - 20%) and an increase of the reflectance by nearly two orders of magnitude. The former is attributed to the removal of acetyl moieties throughout the volume of the ChNC nanoparticles, while the latter can be attributed an order-of-magnitude increase in the local birefringence upon conversion of chitin into chitosan. Our findings on the optical properties of the fabricated films offer an insight into how nature combines nanoarchitecturing and biomaterials to produce structural coloration; it suggests that natural systems often use composites to expand upon hierarchical motifs to enhance the overall optical performance of the material. The methods presented in this work provide a way to harness chitin, a renewable and abundant bio-resource, for sustainable and bio-degradable photonic materials.

4 Experimental Methods

All reagents were of analytical grade and purchased from Fisher Chemicals (FSH International, USA), unless stated otherwise. Milli-Q water was used throughout this work (Synergy UV water purification system, Merck, Germany).

4.1 Isolation of chitin

To isolate fungal chitin from mushroom biomass, a modified extraction procedure was used.[37] Common white mushrooms (*Agaricus Bisporus*, acquired from a local supplier) were washed under warm water, before boiling in water for one hour and finally collecting with a cheese cloth. The cleaned mushrooms were then blended in water using a household stick blender, yielding a purée, which was further boiled in water for an hour. The solids were then collected and pressed again through a cheese cloth to yield a brownish-grey pulp, which was then chemically treated by a two-step alkaline-bleach process: (i) 100 g of the pulp was treated with aqueous NaOH (3 M, 200 mL) and $NaBH_4$ (0.5 wt%, Acros Organics) at 80°C for 3 h. The reaction mixture was subsequently centrifuged (25,000 g, 30 min, 4 °C, Sorvall Lynx 6000)

and the obtained pellet dispersed in Milli-Q water. This washing procedure was repeated three times. (ii) Then, 100 g of the pellet was treated with 300 mL of hydrogen peroxide solution (2.5 wt%, pH~11, set with NaOH) at 80°C for 2h. The solids were collected and purified by centrifugation, as above. The steps (i) and (ii) were repeated once more, followed by collecting the purified chitin by vacuum filtration. The chitin was washed with Milli-Q water to afford a wet white cake. Purification was concluded with dialysis against Milli-Q water for 5 days after which the chitin was stored at 4 °C.

4.2 Preparation of ChNC suspensions

Fungal chitin nanocrystals (f-ChNCs) were obtained using a modified version of a previously reported procedure.[15] The purified fungal chitin (10 g) was refluxed in aqueous HCl solution (3 M HCl, 60 ml/$g_{dry\ chitin}$, 100 °C) for 180 min. The reaction was then quenched by threefold dilution with ice-cold water. The solids were collected by centrifugation (25,000 g, 30 min, 4 °C), and dispersed in Milli-Q. This washing step was repeated followed by dialysis for 5 days against Milli-Q water. The resulting dilute fungal ChNC suspension (1.0 wt%) was then dialyzed against aqueous HCl solution (0.6 mM) until the conductivity in the dialysis bath stopped changing overnight. The suspension was then tip sonicated (6.75 s/mL, at 1 wt%) using 30% amplitude (Fischer Sonic Dismembrator, 500 W) and vacuum-filtered (8.0 and 0.8 µm nitrocellulose filter paper, Millipore, Germany). The f-ChNC suspension was then concentrated to 8.81 ± 0.06 wt%, using a rotary evaporator operating at 50 °C. A drop of chloroform was added to prevent bacterial growth and the suspension was stored at 4 °C prior to use.

The shrimp ChNC suspension (s-ChNC) was prepared according to a previously reported method.[15] Briefly, the shrimp chitin was hydrolyzed in 3.0 M HCl for 270 mins at reflux and the resulting suspension was collected by centrifugation (25,000 g, 30 min, 4 ºC). The pellet was redispersed in Milli-Q and centrifugation applied again and dialyzed against Milli-Q. The ionic strength and pH were set by dialysis of 1.0 wt% ChNC suspension against 0.5 mM aqueous HCl solution. The s-ChNC suspension was then

concentrated to 12.87 ± 0.05 wt%, using a rotary evaporator operating at 50 °C. A drop of chloroform was added to prevent bacterial growth and the suspension was stored at 4 °C prior to use.

Note that for the study of the effects of added NaCl and HCl on the color of the films (Figure 2), the suspensions were instead extensively dialyzed against Milli-Q water, followed by dilution with appropriate amounts of NaCl and HCl solution.

4.3 Evaluation of liquid crystalline behavior of ChNC suspensions

The liquid crystalline behavior was investigated by preparing a dilution series of f-ChNC suspension (1.00 – 5.00 wt%) and loading into a set of round glass capillaries (1.3 mm inner diameter). The capillaries were then sealed using wax and left standing vertically and undisturbed for two weeks, after which they were photographed (Nikon D3200, AF-S DX NIKKOR 18-55mm f/3.5-5.6G VR lens) by placing the capillaries between crossed linear polarizers with rear illumination. The volume percent of the anisotropic phase was defined as the ratio of the height of the anisotropic phase (which appears bright in photographs), over the total height of the suspension (**Figure S4A**). These capillaries were then examined by polarized optical microscopy in transmission mode with the sample placed between crossed linear polarizers (Nikon SLWD 20x/0.30, Zeiss Axio inverted microscope). All the images were analyzed using ImageJ software. The pitch of the chiral nematic phase, as measured by optical microscopy, was defined as twice the periodicity of the fingerprint pattern (**Figure S4B)**. The mean value was calculated from several images per capillary.

4.4 Casting of photonic ChNC films

To obtain ChNC films, suspensions at 2.0 wt% (3.0 g for f-ChNC and 4.0 g for s-ChNC) were dried in polystyrene Petri dishes (35 mm diameter, non-treated PS, ref. 430588, Corning VWR, USA) at room temperature over several days in a ventilated cupboard, unless otherwise stated. Generally films did not stick to the Petri dish and could be peeled off.

4.5 Conversion of chitin to chitosan

Flakes of ChNC films were converted to chitosan by immersing ChNC in an aqueous NaOH solution (50 wt%, 90 °C, 8h). Treated ChNC film flakes were then extensively washed with Milli-Q water until at neutral pH and left to dry under ambient conditions in polystyrene Petri dishes. The flakes generally stuck to the Petri dish and were difficult to remove. Using non-stick hydrophobic surfaces was not found to be beneficial, as the drying films curled up. As a control, applying an equivalent thermal treatment in water did not induce any notable changes to ChNC films.

4.6 Optical characterization of photonic films

The optical response of the ChNC films was characterized using a custom optical microscope (Axio Scope A.1, Zeiss) in bright-field reflection (epi-illumination) mode. Crossed polarization (XP) measurements were collected between two linear polarizers (WP25M-UB, Thorlabs). Left and right circular polarization measurements (LCP, RCP) were collected by filtering reflected light through a quarter-wave plate (B-Halle) followed by a linear polarizer (WP25M-UB, Thorlabs). Images and spectra were collected from flakes originating from the central regions of films to avoid coffee-ring edge effects. All micrographs were obtained using an IDS camera (UI-3580LE) with a 10x objective (Zeiss EC Epiplan-Apochromat 10x/0.3 HD DIC 422642-9960). The color balance was set against a standard white diffuser (USRS-99-010, Labshare). Micro-spectroscopy was typically performed by collecting reflected light using an optical fiber (core diameter 200 μm, FC-UVIR200-2, Avantes) in confocal configuration, which was coupled to a spectrometer (AvaSpec-HS2048, Avantes). For Figure 2, a wider optical fiber was used (core diameter 1000 μm, FC-UV1000-2-SR, Avantes) to obtain the optical response over a larger area. Spectra were normalized to a silver mirror (PF10-03-P01, Thorlabs). All the presented optical spectra are smoothed via a moving average of the nearest 9 neighbors, corresponding to a wavelength window of 5 nm. CIE 1931 chromaticity diagram calculated from XP spectra using the Color package (v. 0.4.1) in Python.[38]

Photographs were obtained using a Nikon DSLR camera (D3200, AF-S DX NIKKOR 18-55mm f/3.5-5.6G VR lens).

4.7 Structural characterization of helicoidal films

Samples for scanning electron microscopy were prepared by breaking films into flakes by pulling them apart to favor crack propagation. The flakes were mounted on an aluminum stub using carbon tape and sputter coated with 10 nm of Au/Pd (Quorum Q150T ES). Imaging was performed using MIRA 3 Scanning electron microscope (Tescan) scanning electron microscope, operating at high vacuum mode at 3-5 kV with a 3-5 mm working distance using in-beam SEM detector. The pitch was measured directly from the cross-sectional images and are reported as the mean value and the standard deviation.

Supporting Information

Supporting Information is appended below. Raw data relating to this publication is freely available from the University of Cambridge data repository.

Acknowledgements

This work was supported by the European Research Council [ERC-2017-POC 790518], the BBSRC [BB/K014617/1, BB/V00364X/1], the EPSRC [EP/N509620/1, EP/L015978/1], Marie Skłodowska-Curie grant agreement [No. 722842], and Lord Lewis Research Studentship in Chemistry, Erasmus + traineeship (NLMAASTRI01). The authors thank Dr Heather Greer for help with performing TEM and SEM measurements, and Matthew Pond for help with technical laboratory details. The authors are grateful to the Duer research group for their help with solid state NMR experiments. The authors are grateful for Cambridge Advanced Imaging Centre for allowing to use their facilities.

Received: ((will be filled in by the editorial staff))
Revised: ((will be filled in by the editorial staff))
Published online: ((will be filled in by the editorial staff))

References

[1] M. Eder, S. Amini, P. Fratzl, *Science* **2018**, *362*, 543.
[2] J. M. Allwood, J. M. Cullen, M. A. Carruth, D. R. Cooper, M. McBrien, *Allwood, J: Sustainable Materials without the Hot Air: Making Buildings, Vehicles and Products Efficiently and with Less New Material*, UIT Cambridge LTD, Cambridge, **2015**.
[3] P. Fratzl, R. Weinkamer, *Prog. Mater. Sci.* **2007**, *52*, 1263.

[4] Y. Politi, L. Bertinetti, P. Fratzl, F. G. Barth, *Philos. Trans. R. Soc. Math. Phys. Eng. Sci.* **2021**, *379*, 20200332.
[5] M. Rinaudo, *Prog. Polym. Sci.* **2006**, *31*, 603.
[6] A. C. Neville, *Biology of the Arthropod Cuticle*, Springer Berlin, Heidelberg, **1975**.
[7] J. C. Weaver, G. W. Milliron, A. Miserez, K. Evans-Lutterodt, S. Herrera, I. Gallana, W. J. Mershon, B. Swanson, P. Zavattieri, E. DiMasi, D. Kisailus, *Science* **2012**, *336*, 1275.
[8] S. Caveney, J. W. S. Pringle, *Proc. R. Soc. Lond. B Biol. Sci.* **1971**, *178*, 205.
[9] M. Mitov, *Soft Matter* **2017**, *13*, 4176.
[10] B. D. Wilts, H. M. Whitney, B. J. Glover, U. Steiner, S. Vignolini, *Mater. Today Proc.* **2014**, *1*, 177.
[11] E. Lizundia, T.-D. Nguyen, R. J. Winnick, M. J. MacLachlan, *J. Mater. Chem. C* **2021**, *9*, 796.
[12] J. Hou, B. E. Aydemir, A. G. Dumanli, *Philos. Trans. R. Soc. Math. Phys. Eng. Sci.* **2021**, *379*, 20200331.
[13] J.-F. Revol, H. Bradford, J. Giasson, R. H. Marchessault, D. G. Gray, *Int. J. Biol. Macromol.* **1992**, *14*, 170.
[14] J.-F. Revol, R. H. Marchessault, *Int. J. Biol. Macromol.* **1993**, *15*, 329.
[15] A. Narkevicius, L. M. Steiner, R. M. Parker, Y. Ogawa, B. Frka-Petesic, S. Vignolini, *Biomacromolecules* **2019**, *20*, 2830.
[16] E. Belamie, P. Davidson, M. M. Giraud-Guille, *J. Phys. Chem. B* **2004**, *108*, 14991.
[17] R. H. Marchessault, F. F. Morehead, N. M. Walter, *Nature* **1959**, *184*, 632.
[18] S. Matsumura, S. Kajiyama, T. Nishimura, T. Kato, *Small* **2015**, *11*, 5127.
[19] L. Onsager, *Ann. N. Y. Acad. Sci.* **1949**, *51*, 627.
[20] T. G. Parton, R. M. Parker, G. T. van de Kerkhof, A. Narkevicius, J. S. Haataja, B. Frka-Petesic, S. Vignolini, *Nat. Commun.* **2022**, *13*, 2657.
[21] M. Chiappini, S. Dussi, B. Frka-Petesic, S. Vignolini, M. Dijkstra, *J. Chem. Phys.* **2022**, *156*, 014904.
[22] Y. Bouligand, *C. R. Acad. Sci. (Paris)* **1965**, *261*, 3665.
[23] H. D. Vries, *Acta Crystallogr.* **1951**, *4*, 219.
[24] H. L. Leertouwer, B. D. Wilts, D. G. Stavenga, *Opt. Express* **2011**, *19*, 24061.
[25] B. Frka-Petesic, G. Kamita, G. Guidetti, S. Vignolini, *Phys. Rev. Mater.* **2019**, *3*, 045601.
[26] B. Zhu, V. E. Johansen, G. Kamita, G. Guidetti, M. M. Bay, T. G. Parton, B. Frka-Petesic, S. Vignolini, *ACS Nano* **2020**, *14*, 15361.
[27] A. Mendoza-Galván, E. Muñoz-Pineda, K. Järrendahl, H. Arwin, *Opt. Mater. Express* **2016**, *6*, 671.
[28] B. Frka-Petesic, J. Sugiyama, S. Kimura, H. Chanzy, G. Maret, *Macromolecules* **2015**, *48*, 8844.
[29] K. R. Krishna Iyer, P. Neelakantan, T. Radhakrishnan, *J. Polym. Sci. Part -2 Polym. Phys.* **1968**, *6*, 1747.
[30] A. G. Dumanli, H. M. van der Kooij, G. Kamita, E. Reisner, J. J. Baumberg, U. Steiner, S. Vignolini, *ACS Appl. Mater. Interfaces* **2014**, *6*, 12302.
[31] C. Honorato-Rios, A. Kuhnhold, J. R. Bruckner, R. Dannert, T. Schilling, J. P. F. Lagerwall, *Front. Mater.* **2016**, *3*, 21.
[32] D. E. Azofeifa, H. J. Arguedas, W. E. Vargas, *Opt. Mater.* **2012**, *35*, 175.
[33] T.-D. Nguyen, M. J. MacLachlan, *Adv. Opt. Mater.* **2014**, *2*, 1031.
[34] T.-D. Nguyen, B. U. Peres, R. M. Carvalho, M. J. MacLachlan, *Adv. Funct. Mater.* **2016**, *26*, 2875.
[35] M. N. V. Ravi Kumar, *React. Funct. Polym.* **2000**, *46*, 1.
[36] L. A. Hadwiger, *Plant Sci.* **2013**, *208*, 42.
[37] N. Lin, S. Zhao, L. Gan, P. R. Chang, T. Xia, J. Huang, *Carbohydr. Polym.* **2017**, *173*, 610.
[38] T. Mansencal, M. Mauderer, M. Parsons, N. Shaw, K. Wheatley, S. Cooper, J. D. Vandenberg, L. Canavan, K. Crowson, O. Lev, K. Leinweber, S. Sharma, T. J. Sobotka, D. Moritz, M. Pppp, C. Rane, P. Eswaramoorthy, J. Mertic, B. Pearlstine, M. Leonhardt, O. Niemitalo, M. Szymanski, M. Schambach, S. Huang, M. Wei, N. Joywardhan, O. Wagih, P. Redman, J. Goldstone, S. Hill, *Colour 0.3.16*, Zenodo, **2020**.

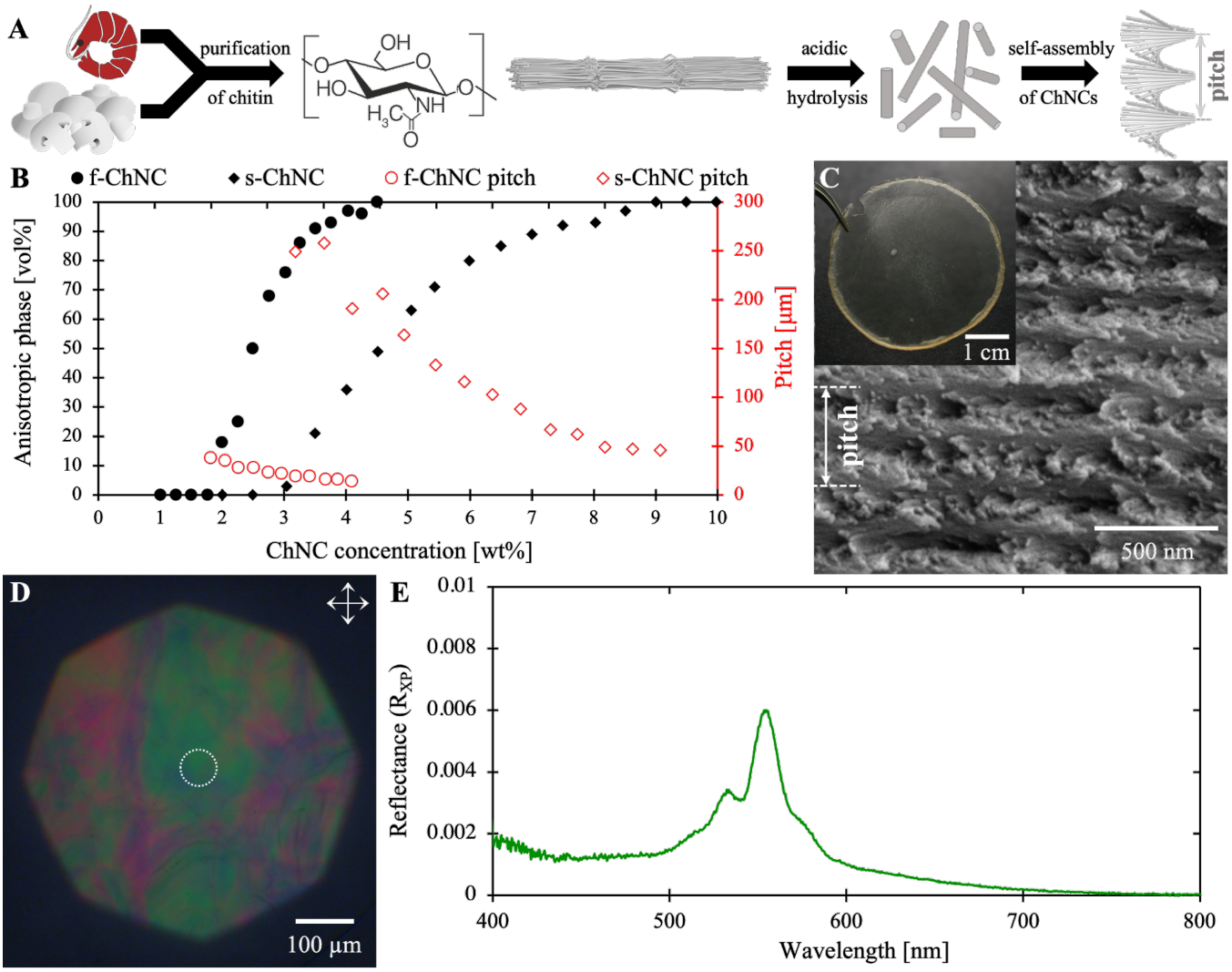

Figure 1. Structurally colored ChNC films produced via the self-assembly of chitin nanocrystals. (**A**) A schematic illustrating the extraction, formation and self-assembly of chitin nanocrystals. **(B)** Proportion of anisotropic phase (black full symbols) and the pitch (red open symbols) for ChNC suspension derived from fungal chitin (f-ChNC, circles) and shrimp chitin (s-ChNC, diamonds). **(C)** Cross-sectional SEM image of a f-ChNC film, showing a pitch ($p = 360 \pm 90$ nm) compatible with structural color in the visible range. A photograph of the film is shown in the inset, which appears colorless by eye. **(D)** Crossed polarized micrograph in epi-illumination of the f-ChNC film revealing faint structural coloration. **(E)** Corresponding micro-spectroscopy of the film (white dotted circle in C) confirming a weak, narrow peak in the reflection spectrum.

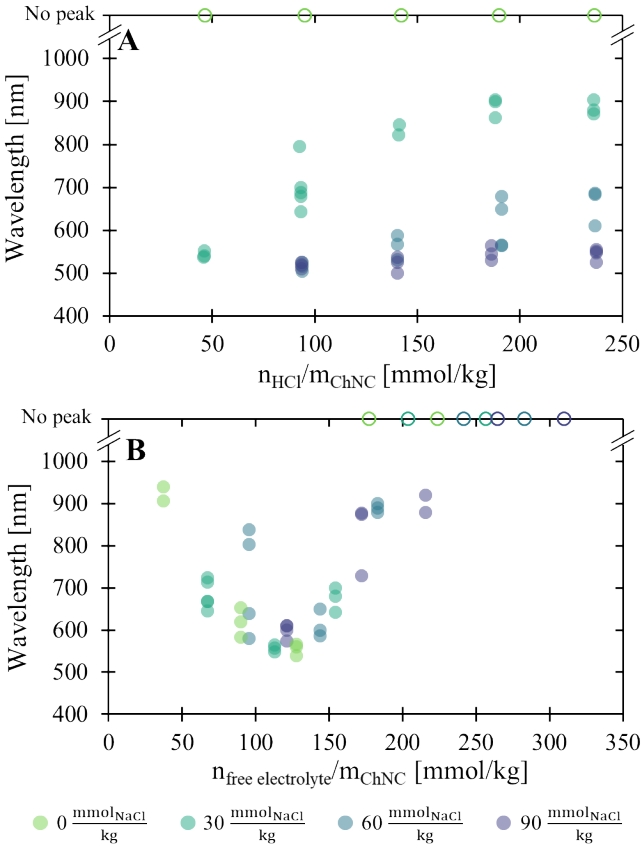

Figure 2. Tuning of the reflection peak wavelength of f-ChNC films. (**A**) Effect of the ratio of HCl to f-ChNC, added after extensive dialysis against Milli-Q water and the addition of increasing amounts of NaCl. (**B**) Effect of additional monovalent ions (HCl or NaCl) to a fully protonated f-ChNC suspension (achieved by prior addition of 246 mmol/kg of HCl). Full circles denote the wavelength of peaks reflection, while open circles denote ChNC films where a reflection peak was not observed within the measurement window of the spectrometer.

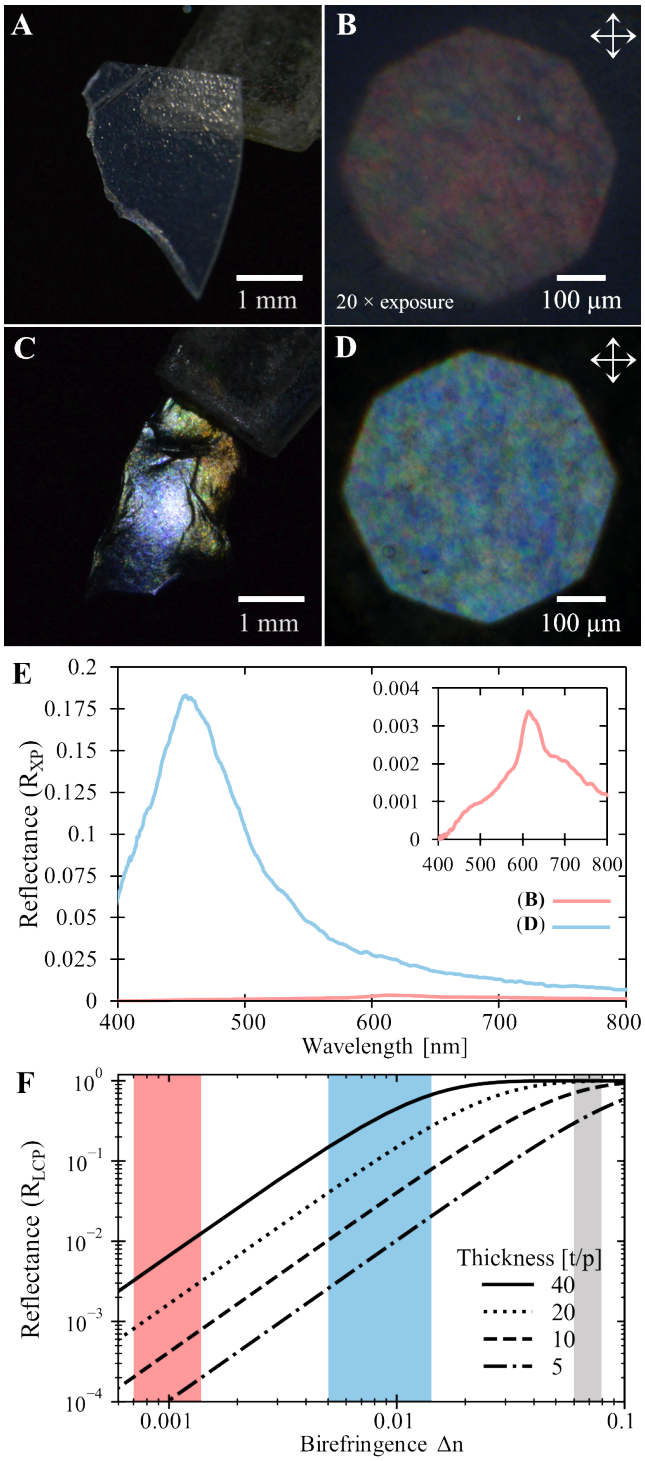

Figure 3. Enhancing structural coloration by alkaline post-treatment of ChNC films. **(A)** Photograph of an apparently colorless flake from an f-ChNC film. **(B)** Optical microscopy of the flake in (A) using crossed linear polarizers. Increasing the exposure 20× reveals the presence of weak red/green structural coloration. **(C)** Photograph of a f-ChNC film flake after alkaline treatment, exhibiting strong blue/green coloration. **(D)** Optical microscopy image of the flake in (C), confirming higher reflectance and a blue-shift of the reflected color. **(E)** Reflection spectra under crossed polarizers corresponding to (B) and (D) showing the weak red-green reflectance for the original f-ChNC film (*red line,* enlarged in inset spectrum) and the more intense blue-shifted reflectance after alkaline post-treatment (*blue line*). (**F**) The maximum reflectance for helicoidal structures with varied thickness and birefringence, calculated using de Vries theory. Estimated birefringence ranges are shown as shaded areas for the untreated f-ChNC film (*red*) and the alkaline treated film (*blue*). For comparison, the estimated birefringence range for photonic cellulose nanocrystal (CNC) films is also indicated (*gray*).

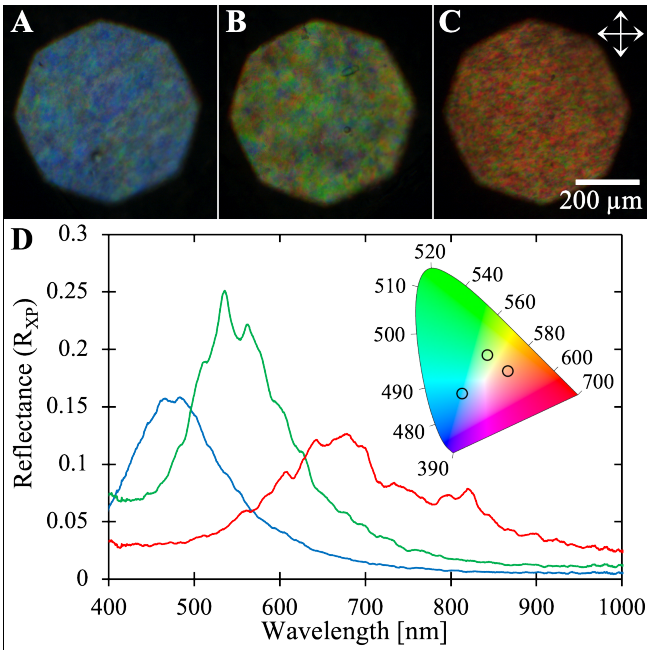

Figure 4. Tuning the structural coloration of post-treated f-ChNC films. **(A-C)** Alkaline treatment on f-ChNC films cast with 235 $mmol_{HCl}$/kg and 90, 60, or 30 $mmol_{NaCl}$/kg, produced structurally colored films displaying (A) blue, (B) green, and (C) red color, respectively. (**D**) Reflection spectra between crossed polarizers for the films in (A-C). Inset: CIE 1931 chromaticity diagram. Open circles denote positions of the blue, green and red films, with respective *x*-*y* coordinates of (0.21, 0.27), (0.33, 0.44) and (0.42, 0.37).

Supporting Information

Revealing the Structural Coloration of Self-Assembled Chitin Nanocrystal Films

*Aurimas Narkevicius, Richard M. Parker, Jordi Ferrer-Orri, Thomas G. Parton, Zihao Lu, Gea T. van de Kerkhof, Bruno Frka-Petesic, and Silvia Vignolini**

Dr. Aurimas Narkevicius, Dr. Richard M. Parker, Jordi Ferrer-Orri, Thomas G. Parton, Zihao Lu, Dr. Gea T. van de Kerkhof, Dr. Bruno Frka-Petesic, Prof. Silvia Vignolini
Yusuf Hamied Department of Chemistry, University of Cambridge, Lensfield Road, Cambridge, CB2 1EW, United Kingdom

E-mail: sv319@cam.ac.uk

S1. Extended Experimental Methods

Transmission Electron Microscopy (TEM)

The samples were prepared by depositing a drop of dilute ChNC suspension (0.001 wt%) on a glow-discharged carbon-coated copper grid. After 90 seconds, the excess liquid was blotted using filter paper, followed by staining with uranyl acetate (aqueous, 2.00 wt%) for 90 seconds. The grid was dried in air and then observed using either (i) a Tecnai G2 transmission electron microscope (FEI/ThermoFisher Scientific) operating at 200 kV and using a 20 mm objective aperture to improve contrast, with an ORCA HR CCD camera (AMT Corp.) for micrographs or (ii) Talos F200X G2 scanning transmission electron microscope (FEI/ThermoFicher Scientific) operating at 200 kV and a CCD camera.

Atomic Force Microscopy (AFM)

AFM images were obtained by incubating a fully wetting droplet (dilute ChNC suspension of *ca.* 0.001 wt%) on freshly cleaved mica for 2 minutes, then rinsing with Milli-Q water and drying first with a flow of N_2 and then in an oven at 50 ºC for 1 hour. The measurements were obtained using a scanning probe microscope (Agilent 5500 SPM) in tapping mode with a commercial AFM probe (OTESPA-R3). The 4 x 4 μm size areas were scanned at a resolution of 1024 points per line, with a rate of 0.6 Hz. The data was processed using Gwyddion 2.8 software.

Solid-state nuclear magnetic resonance spectroscopy (ssNMR)

Cross-polarization magic angle spinning ^{13}C-ssNMR spectroscopy was performed at room temperature using an Ultrashield 400 spectrometer (Bruker) with a rotor spinning at 14 kHz. Glycine was used as a reference. A relaxation delay of 2 s and a contact time of 1 ms were used for the acquisition of spectra. The data was smoothed using the Savitzky-Golay method of third-degree polynomial with a window size of 51. Samples were freeze-dried before analysis.

Powder X-ray Diffraction (pXRD)

The diffractograms were recorded using freeze dried material at angles (2θ) from 5º to 50º at 40 kV, 30 mA using Empyrean powder diffractometer (Malvern Panalytical). The data was smoothed using the Savitzky-Golay method of third-degree polynomial with a window size of 51.

FTIR spectroscopy

The spectra were collected in the 600-4000 cm^{-1} range with 64 repeats and a resolution of 4 cm^{-1} using a Spectrum 100 ATR spectrometer (PerkinElmer). The measurements were collected on freeze-dried samples.

Conductometric Titration

For data showed in Figure S8A, conductometric titration was performed manually by dropwise adding HCl (10 mM, Titripur) into a diluted ChNC suspension (ca. 0.1 wt%). The amount of added acid each time was measured from the mass loss in the syringe containing the acid. The conductivity was determined following each addition (InLab 752-6mm electrode, Mettler Toledo). For data showed in Figure S7B, conductometric titration of f-ChNC suspension was performed after it was fully protonated with an excess of added HCl. This titration was performed using NaOH (10 mM, Titripur) using an automated system (dosing unit 807, conductivity module 856, Metrohm).

Casting of ChNC-PEG films

ChNC-PEG films were prepared by casting a formulation containing f-ChNC suspension (6.0 g at 1 wt%), HCl (328 mmol/g) and NaCl (30 mmol/g) and an appropriate amount of PEG (35 kDa) so that the final films would contain 0 – 20 wt% PEG.

S2. Discussion of reflection from a thin helicoidal structure

An ideal helicoidal structure of infinite thickness has a theoretical limit of 50% reflectance of unpolarized light due to the chirality of the helicoidal nanostructure (i.e., 100% LCP reflectance and 0% RCP reflectance for an ideal photonic ChNC film). As such, they can be outperformed by achiral photonic crystals (e.g., self-assembled colloidal opals or multilayers produced by top-down fabrication), which can reflect up to 100% of unpolarized light. Nevertheless, selective reflection of up to 50% of incident unpolarized light is sufficient to produce vibrant coloration.

In practice, the reflectance from helicoidal ChNC films depends on their (finite) thickness, pitch and effective birefringence. As such, the peak LCP reflectance from a thin helicoidal structure can be calculated using Equation 1 in the article. This equation is corollary of the work of de Vries,[1] but is not explicitly stated in that work, so a derivation is provided below using the same notation.

The optical response of a helicoidal structure can be predicted by modelling the structure as a stack of birefringent layers with a constant twist angle between each layer. In a given layer, the permittivity along the principal axes are ε_1 and ε_2, from which we define the average permittivity

$$\varepsilon = \frac{1}{2}(\varepsilon_1 + \varepsilon_2)$$

and a relative birefringence α, given by

$$\alpha = \frac{\varepsilon_2 - \varepsilon_1}{2\varepsilon}.$$

By solving the electromagnetic boundary conditions between layers, it can be shown that the modes of a helicoidal multilayer with pitch p are elliptically polarized, with an effective "refractive index" parameter m, given by Equation 12 in the work of de Vries[1]:

$$m^4 - 2m^2(\varepsilon + \lambda^2/p^2) + (\varepsilon_1 - \lambda^2/p^2)(\varepsilon_2 - \lambda^2/p^2) = 0$$

This equation can be made dimensionless by defining $m' = m/\sqrt{\epsilon}$ and relative wavelength $\lambda' = \lambda/(p\sqrt{\epsilon})$:

$$m'^4 - 2m'^2(1 + \lambda'^2) + (1 - \lambda'^2 - \alpha)(1 - \lambda'^2 + \alpha) = 0$$

The ellipticity of the polarization of the corresponding electromagnetic mode is given by

$$f = \frac{1 - \lambda'^2 - \alpha - m'^2}{2m'\lambda'}.$$

It is also convenient to define a factor $q = m' + \lambda' f$. The equation for m' above can be considered a quadratic equation in m'^2 with two possible solutions (the equation is quartic in m', but the difference between $\pm|m'|$ for each solution is only a change in the propagation direction). Explicitly, m'^2 is given by

$$m'^2 = (1 + \lambda'^2) \pm \sqrt{(1 + \lambda'^2)^2 - (1 - \lambda'^2 - \alpha)(1 - \lambda'^2 + \alpha)}$$

When considering the reflection from the helicoidal structure, the smaller solution ($m_1'^2$) is more relevant, as it takes negative values in the bandgap region leading to strong reflection, whereas the larger solution $m_2'^2$ is always positive.

The LCP reflectance from a left-handed helicoidal layer of thickness t and pitch p at normal incidence is given by the following equation:

$$R_{LCP} = \frac{(1-q^2)^2(1-s^2)^2}{(1-q^2)^2(1-s^2)^2 - 16s^2q^2},$$

where s is a phase factor $s = \exp\left(i\frac{2\pi m_1{}'t}{\lambda' p}\right)$ and q is as defined above for $m' = m_1{}'$. At peak reflectance ($\lambda' = 1$), the quadratic equation for m'^2 simplifies to

$$m'^2 = 2\left(1 \pm \sqrt{1 + \left(\frac{\alpha}{2}\right)^2}\right)$$

In experimental systems, the birefringence parameter α is often small (e.g. for the related system of cellulose nanocrystals, $\alpha \approx 0.04$). The expression for m'^2 can therefore be expanded to lowest order in α as

$$m_1'^2 = 2\left(1 - \left(1 + \frac{1}{2}\left(\frac{\alpha}{2}\right)^2\right) + \cdots\right) \approx -\left(\frac{\alpha}{2}\right)^2.$$

Similarly, it can be shown that in this case $f_1 \approx \sqrt{-1}$ and $q_1^2 \approx -1$ so the peak reflectance is given by

$$R_{LCP} \approx \frac{(1-s^2)^2}{(1-s^2)^2 + 4s^2}.$$

As $m_1{}'$ is imaginary, the phase factor s has the form $s = \exp(-z)$ for real z, and the LCP reflectance can be written more elegantly as

$$R_{LCP} = \tanh^2 z = \tanh^2\left(\frac{\pi\ \alpha\ t}{p}\right)$$

Finally, the birefringence α can be written explicitly in terms of refractive indices $n_j = \sqrt{\varepsilon_j}$ as

$$\alpha = \frac{n_2^2 - n_1^2}{n_2^2 + n_1^2}$$

and since $\alpha \ll 1$, this expression simplifies to $\alpha \approx \frac{\Delta n}{n_{avg}}$, where $\Delta n = n_2 - n_1$ and $n_{avg} = \sqrt{\varepsilon}$. Hence the LCP reflectance can be written as

$$R_{LCP} = \tanh^2\left(\frac{\pi\ \Delta n\ t}{n_{avg}\ p}\right).$$

For small reflectance values ($R_{LCP} \ll 1$), this equation simplifies to

$$R_{LCP} = \left(\frac{\pi\ \Delta n\ t}{n_{avg}\ p}\right)^2.$$

The equations for R_{LCP} can also be inverted to give an expression for the birefringence of a domain of a given size and reflectance:

$$\Delta n = \frac{n\ p}{\pi\ t}\tanh^{-1}\sqrt{R_{LCP}} = \frac{n_{avg}\ p}{2\ \pi\ t}\ln\left(\frac{1+\sqrt{R_{LCP}}}{1-\sqrt{R_{LCP}}}\right).$$

It is important to note that the birefringence in the equations above is the effective birefringence of the helicoidal structure Δn_{eff}. For helicoidal ChNC films, the effective birefringence is related to the intrinsic

birefringence of the individual ChNCs Δn_{ChNC} by the equation $\Delta n_{eff} = \Delta n_{ChNC}.S_2$, where S_2 is the nematic order parameter that quantifies the degree of local ordering and ranges from 0 to 1. For helicoidal structures made by colloidal self-assembly, S_2 is expected to be in the range 0.6-0.9,[2] so the intrinsic birefringence is expected to be no more than twice the effective birefringence.

S3. Normalization of reflectance

Experimentally, the maximum measurable reflectance of a chiral nematic structure is dependent on the microscope setup and normalization convention. Reflectance values are typically normalized to a standard reference material; for instance, a silver mirror was used as reference for all spectra in this work. The LCP reflection from a sample was determined by illuminating the sample with unpolarized light and analyzing (i.e. filtering) the reflected light to select the LCP channel. The LCP reflectance, R_{LCP}, was therefore normalized to the LCP reflection from a silver mirror illuminated with unpolarized light. Since a perfect left-handed chiral nematic structure only reflects LCP light and no RCP light, the theoretical total reflectance, R, defined relative to unpolarized illumination, is equal to half the R_{LCP}, thus $R = \frac{1}{2} R_{LCP}$.

The reflection through crossed polarizers (XP) was measured by illuminating the sample with linear polarized light and analyzing the reflected light with a linear polarizer oriented perpendicular to the first polarizer. The XP reflectance, R_{XP}, was normalized to the reflection from a silver mirror between parallel polarizers. When illuminated with linearly polarized light, a perfect left-handed chiral nematic structure (with an associated $R_{LCP} = 1$) will reflect half of the incident light, as linearly polarized light is an equal mixture of LCP and RCP components and the chiral nematic will only reflect the LCP component. The linearly polarized analyzer (whether parallel or crossed relative to the first linear polarizer) then transmits only half of the reflected LCP light and thus only 25% of the incident (linearly polarized) light can reach the detector. The XP reflectance, normalized as described above, should therefore compare to R_{LCP} as $R_{LCP} = 4\, R_{XP}$ (while under unpolarized light, we would get $R = 2\, R_{XP}$). In practice we found that the conversion factor between R_{LCP} and R_{XP} varied between 1 and 4, an observation that we ascribe to possible polarization effects of the beamsplitters within the microscope. To capture the uncertainty associated with this conversion factor, we provided our estimation of Δn for a range of values between 1 and 4.

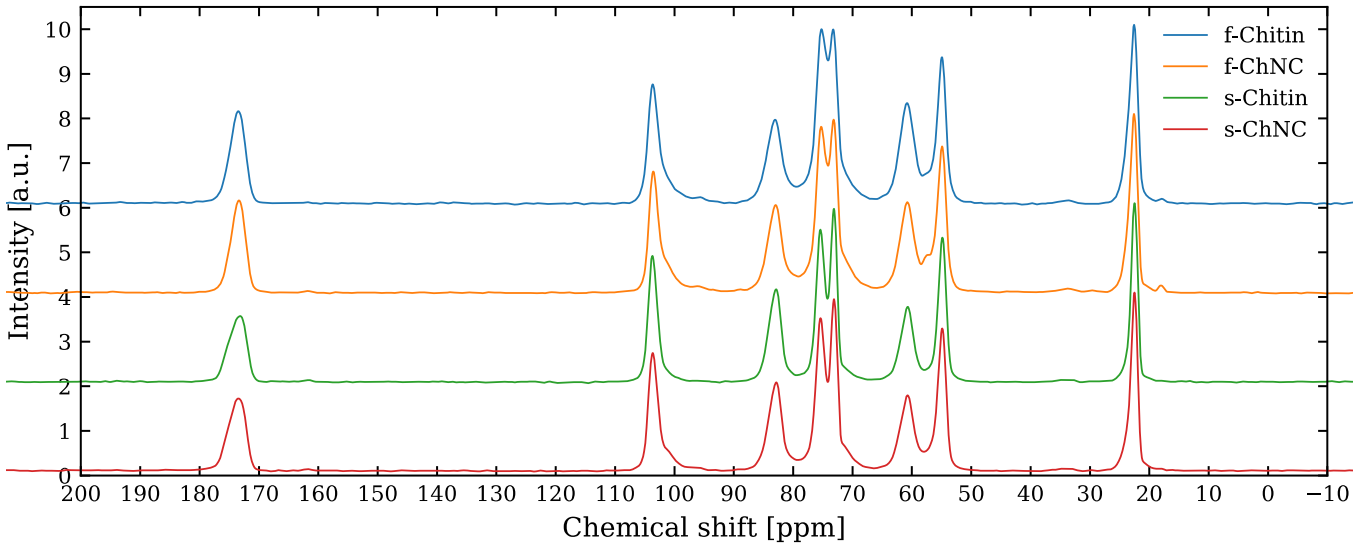

Figure S1. Stacked ^{13}C-ssNMR spectra comparing fungal and shrimp chitin and the corresponding chitin nanocrystals (ChNCs). All four samples – fungal chitin (f-Chitin), fungal ChNC (f-ChNC), shrimp chitin (s-Chitin) and shrimp ChNC (s-ChNC) – correspond to the chitin structure and exhibit good purity.

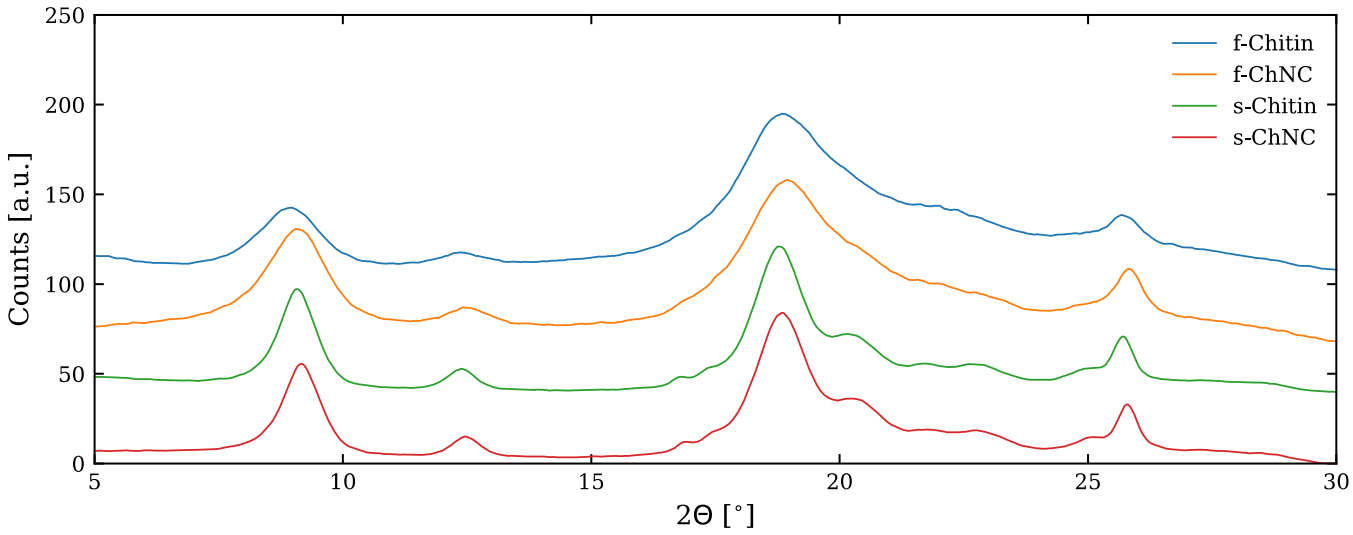

Figure S2. Stacked pXRD diffractograms comparing fungal and shrimp chitin and their corresponding ChNCs. The diffractograms indicate that there is little difference between chitin and the respective ChNCs produced, evidenced by the similar data for both pairs, i.e., fungal chitin (f-Chitin) and fungal ChNC (f-ChNC), and shrimp chitin (s-Chitin) and shrimp ChNC (s-ChNC). However, the fungi-derived materials show broader diffraction peaks suggesting that they are less crystalline than those derived from shrimp.

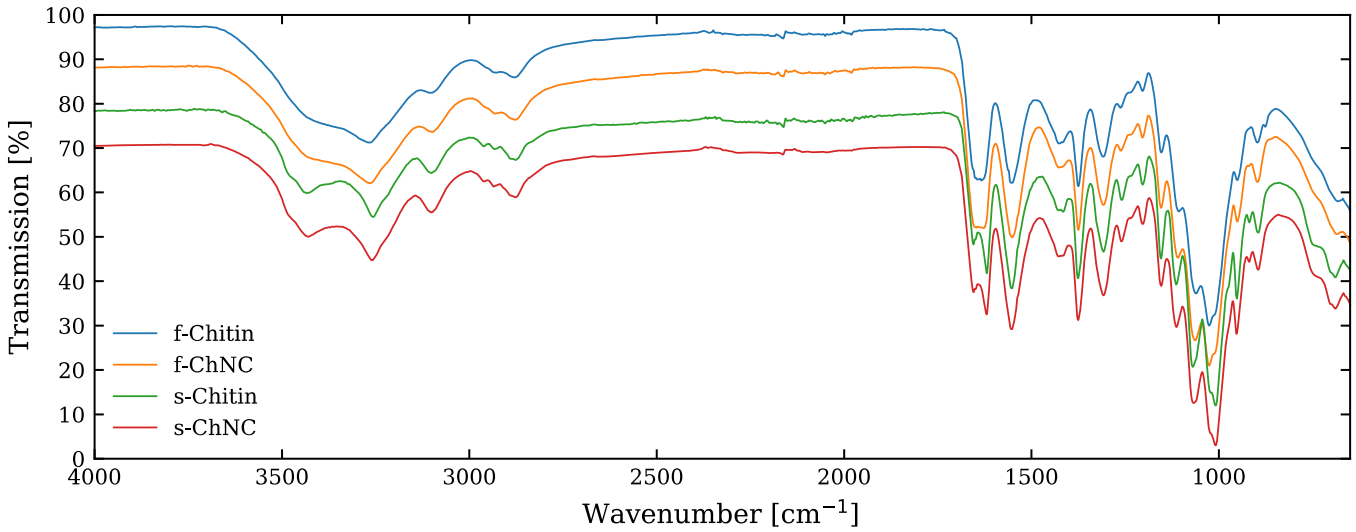

Figure S3. Stacked ATR-FTIR spectra comparing fungal and shrimp chitin and corresponding ChNCs. The two peaks at 1660 and 1620 cm^{-1} correspond to the splitting of the amide carbonyl stretching signal which is associated with the α-chitin crystal structure. While it is very prominent for shrimp chitin (s-Chitin) and shrimp ChNC (s-ChNC) samples, the splitting is hard to resolve for fungal chitin (f-Chitin) and fungal ChNC (f-ChNC) samples. This suggests that fungal derived material is less crystalline than that originating from shrimp.

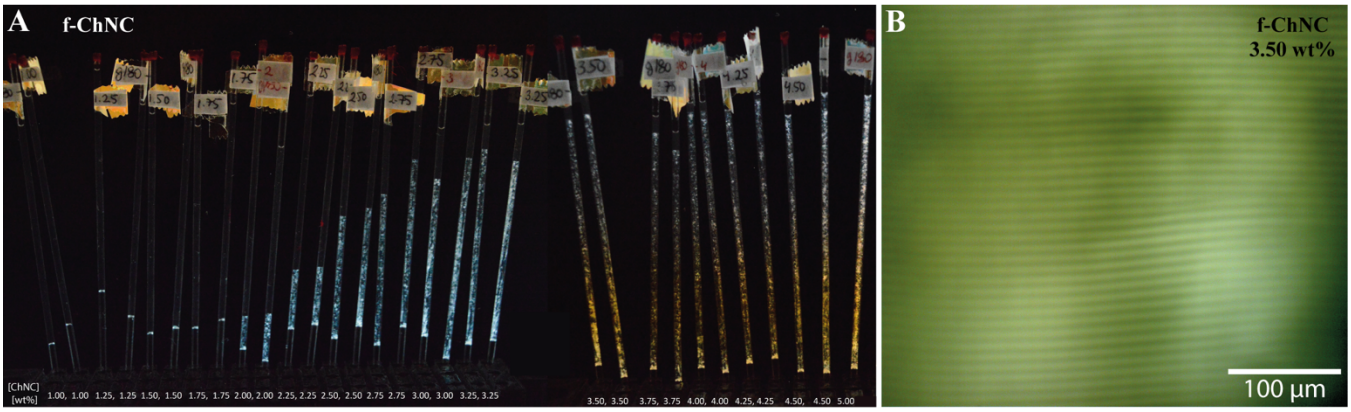

Figure S4. Self-assembly behavior of ChNCs derived from fungi. (**A**) Photograph of capillaries filled with f-ChNC suspension with increasing concentration. **(B)** The fingerprint pattern, characteristic for chiral nematic phase, was imaged by polarized optical microscopy for a 3.50 wt% ChNC suspension.

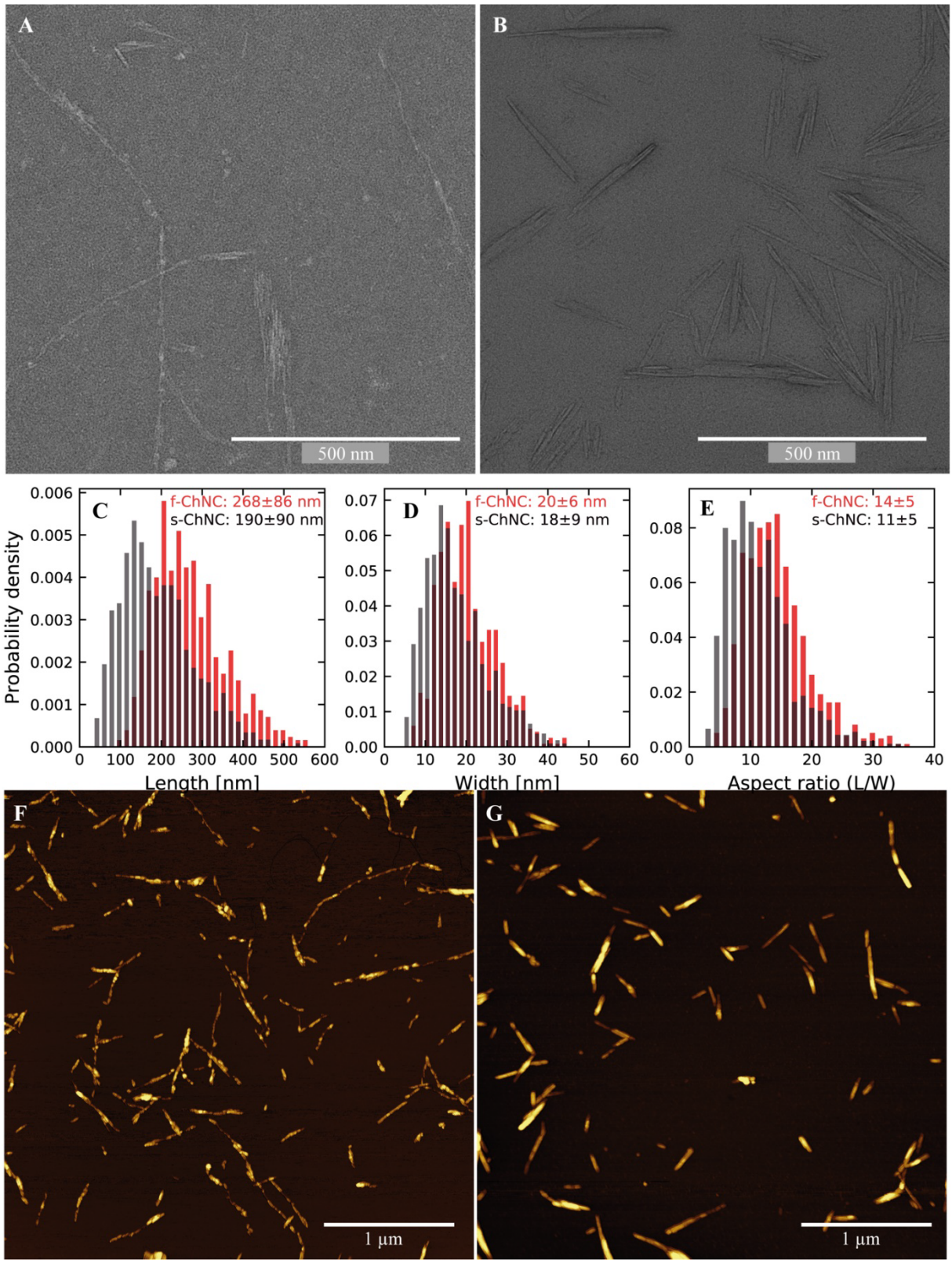

Figure S5. Representative transmission electron micrographs comparing the two sources: (**A**) f-ChNC and (**B**) s-ChNCs. The particles were analyzed using ImageJ software, by manually measuring particle dimensions to obtain statistics on (**C**) length and (**D**) width, allowing for (**E**) individual particle aspect ratios to be calculated. The average and standard deviation for each respective measurement is indicated in the top right corner of the histogram. These measurements reveal that f-ChNC are significantly longer with a larger aspect ratio than s-ChNCs, which agrees with the qualitative observations by atomic force microscopy (AFM), where (**F**) f-ChNC also appear much longer than (**G**) s-ChNC.

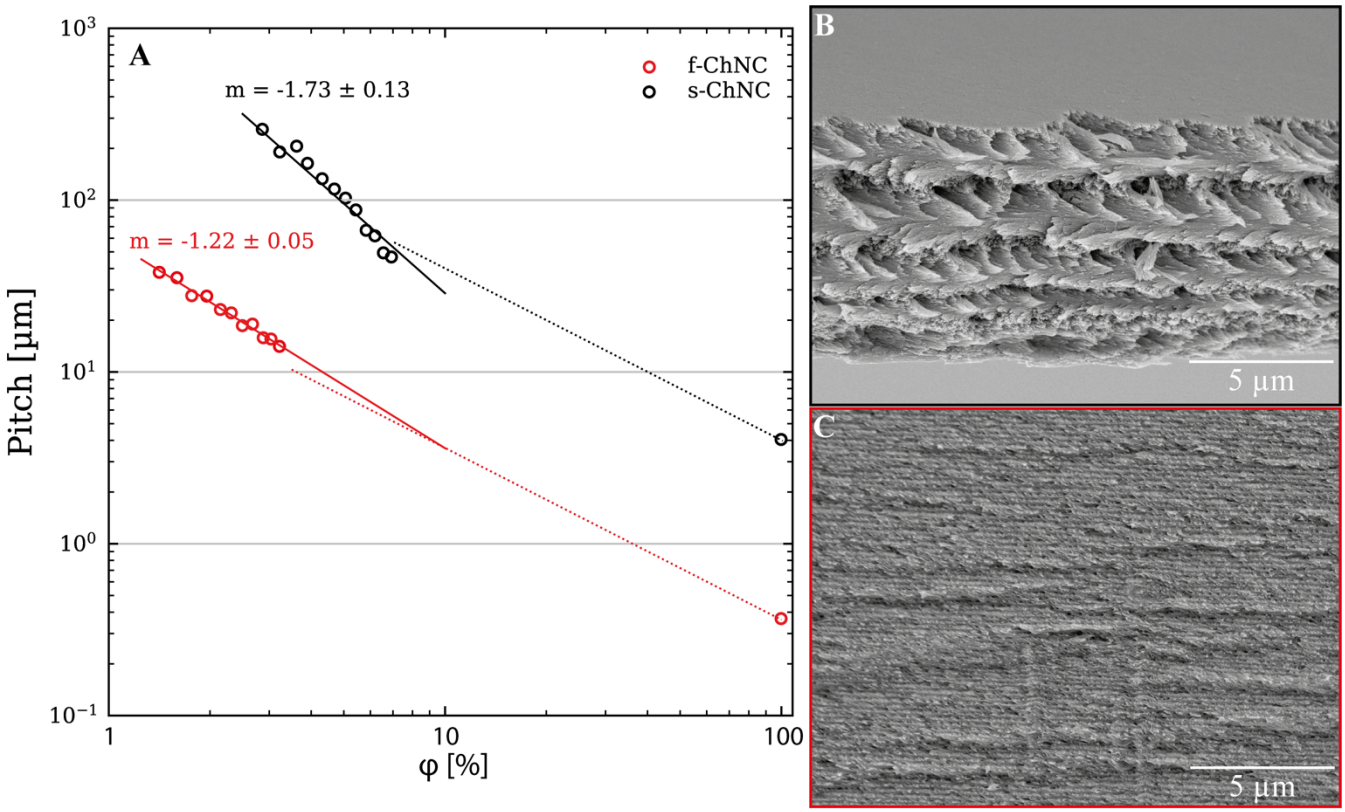

Figure S6. Pitch analysis of ChNCs self-assembled in suspension and after drying to form a film. (**A**) The chiral nematic pitch values at all concentrations except 100 vol% were obtained from the capillaries, (data presented in Figure 1, S4), and were replotted on a log-log scale with the ChNC concentration rescaled to be expressed in volume fraction. Data for s-ChNCs and f-ChNCs are denoted by black circles and red circles respectively. These suspensions are prepared by dialyzis at 1 wt% against 0.6 mM HCl (see Experimental Methods). The evolution of the pitch is represented by the guide lines, with the point of kinetic arrest expected at their intersection. Note that pitch values at 100 vol% are measured by SEM of film cross-sections, with example micrographs provided in (**B**) for s-ChNC and (**C**) for f-ChNC.

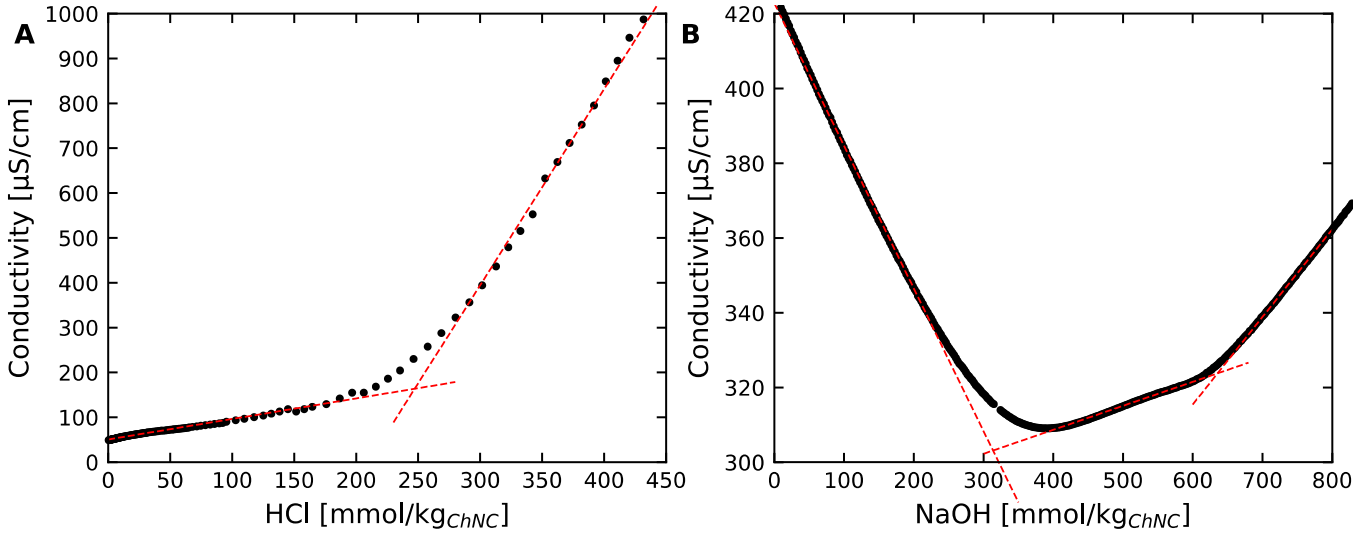

Figure S7. Titration of f-ChNC with HCl and NaOH. (**A)** Titration of f-ChNC suspension using HCl after extensive dialysis against Milli-Q water. Such a suspension can capture up to 246 $mmol_{HCl}$/kg before it becomes fully protonated, as determined where the two lines intersect. This allows for the surface charge to be tuned without altering meaningfully the ionic strength **(B)** Titration of the same f-ChNC suspension using NaOH, starting with an initial excess of added HCl. This titration reveals that the maximum surface charge attainable for f-ChNC suspensions, given by the gap between the two equivalence points, is 330 mmol/kg, as determined from the intersection of the three lines fitted to the experimental data.

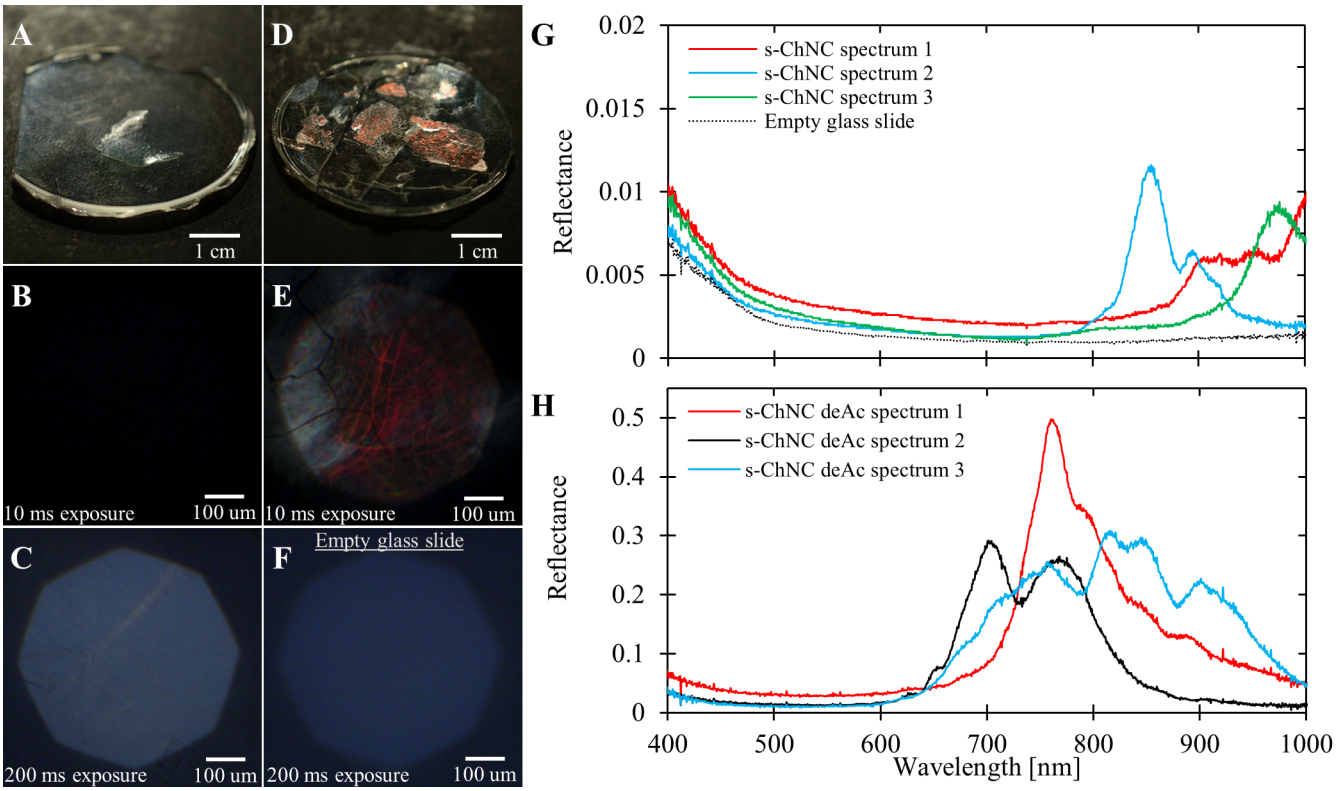

Figure S8. Pitch contraction after alkaline post-treatment. **(A)** Photograph of a flake from an apparently colorless s-ChNC film on a polystyrene Petri dish. The film was prepared by extensively dialyzing s-ChNC suspension against Milli-Q water, followed by adding 100 mmol/kg HCl and 120 mmol/kg NaCl. **(B, C)** Cross polarized optical micrographs of the film in (A) at different camera exposure times**.** (**D**) After an in-situ treatment with concentrated sodium hydroxide, the film becomes red, which is confirmed by optical microscopy in **(E)**. **(F)** POM micrograph obtained using identical conditions as in (C) but of a glass slide without a sample, showing that the blueish tint in (C) was a measurement artefact, also seen in (G) as the weak shoulder in the spectroscopy data (dotted line). (**G**) Three exemplary spectra from s-ChNC films being beyond the visible range. (**H**) Presentation of three typical spectra from s-ChNC flake from the same film after it has been treated with an alkali. The reflectance has increased around 20-fold and the signal has been shifted to lower wavelengths, explaining the presence of some red coloration. Nevertheless, most of the signal remains still outside visible spectrum.

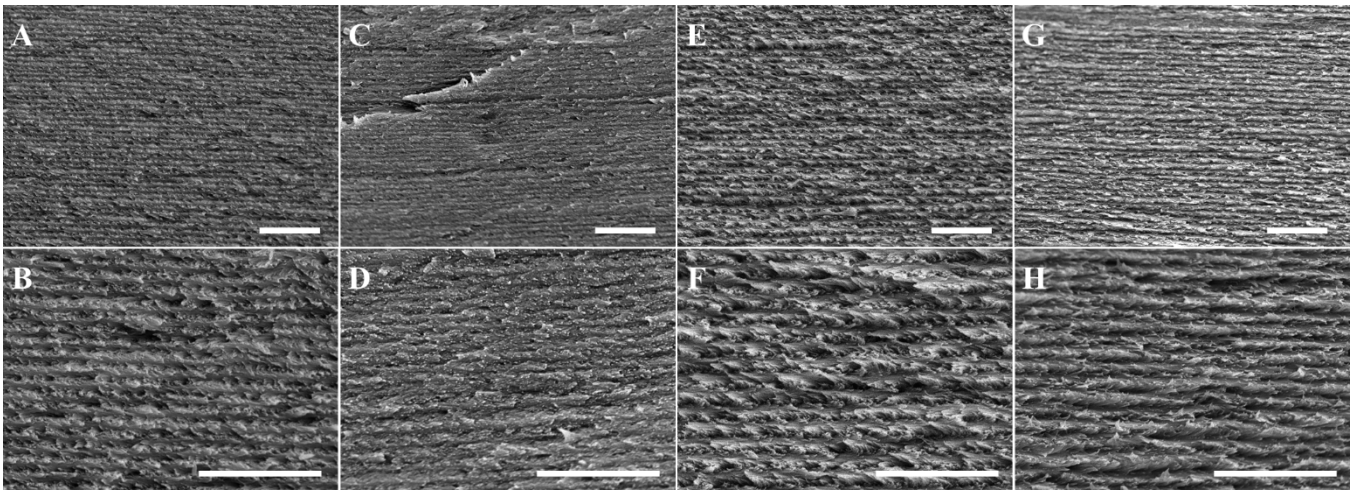

Figure S9. Cross-sectional SEM images of ChNC films before and after in-situ alkaline treatment. (**A, B**) f-ChNC film before alkaline treatment. (**C, D**) f-ChNC film after alkaline treatment (same film, different flake). (**E, F**) s-ChNC film before alkaline treatment. (**G, H**) s-ChNC film after alkaline treatment (same film, different flake). In both cases, the structure is retained with a noticeable reduction in pitch and overall film thickness.

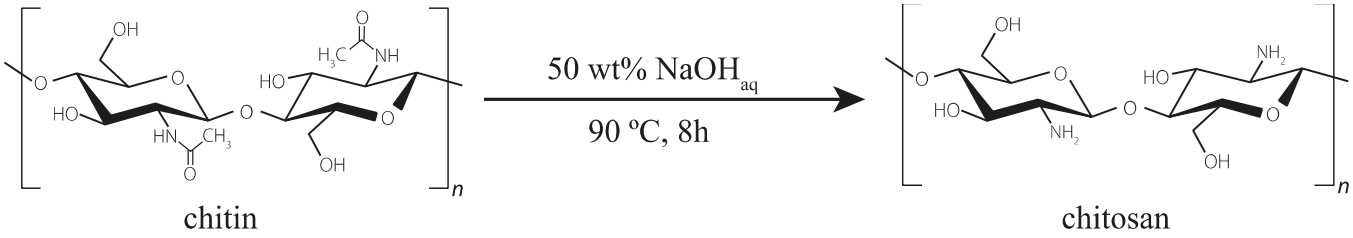

Figure S10. Schematic showing the hydrolysis of chitin to chitosan with concentrated sodium hydroxide.

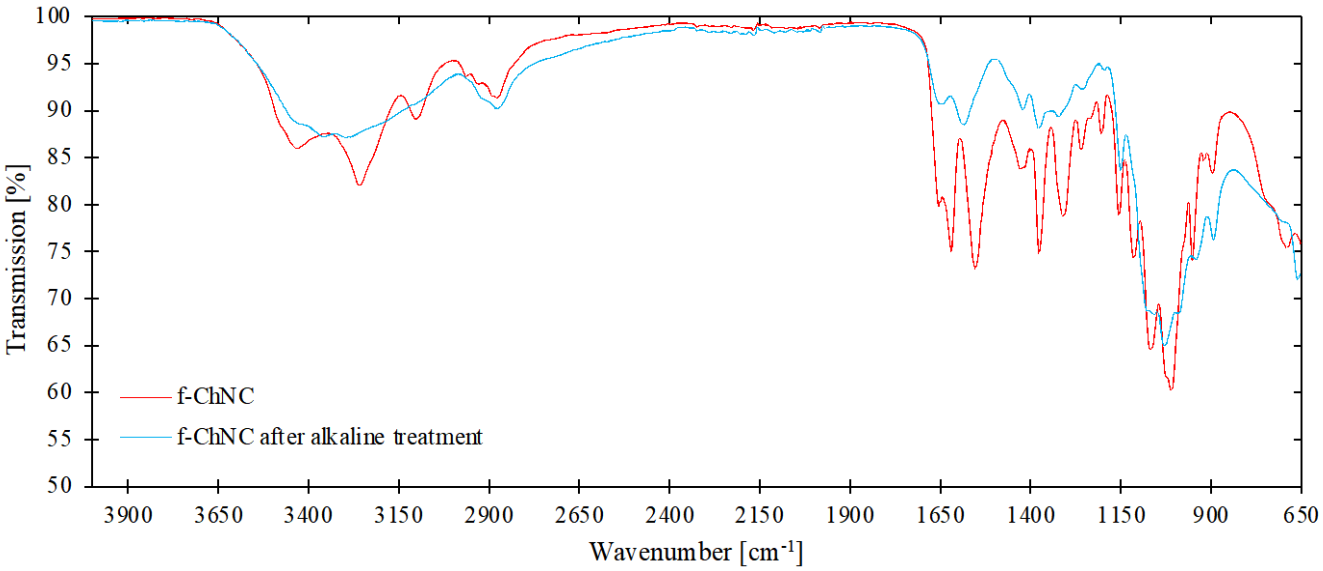

Figure S11. ATR-FTIR spectra of the fungal ChNC film before (*red*) and after (*blue*) alkaline treatment. The peaks at 1554, 1619, and 1656 cm^{-1} are associated with the amide in α-chitin, which after the alkaline treatment have disappeared and are replaced by new peaks at 1585 and 1650 cm^{-1}. This indicates a successful conversion from chitin to chitosan.

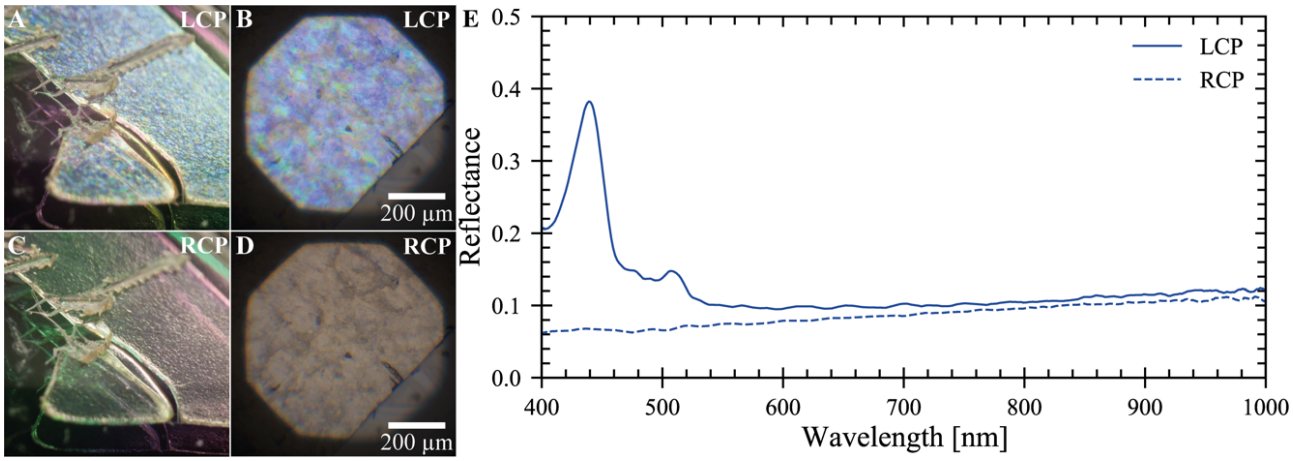

Figure S12. Increased reflectance after the alkaline treatment of solid-state f-ChNC films. (**A**) Macroscopically, structural coloration can be observed by naked eye when selecting for the reflected left circularly polarized (LCP) light. (**B**) The color disappears when collecting only right circularly polarized (RCP) light, consistent with the expected optical behavior of a left-handed helicoidal structure. (**C, D**) Polarized optical microscopy and (**E**) micro-spectroscopy confirms the selective reflection of LCP light.

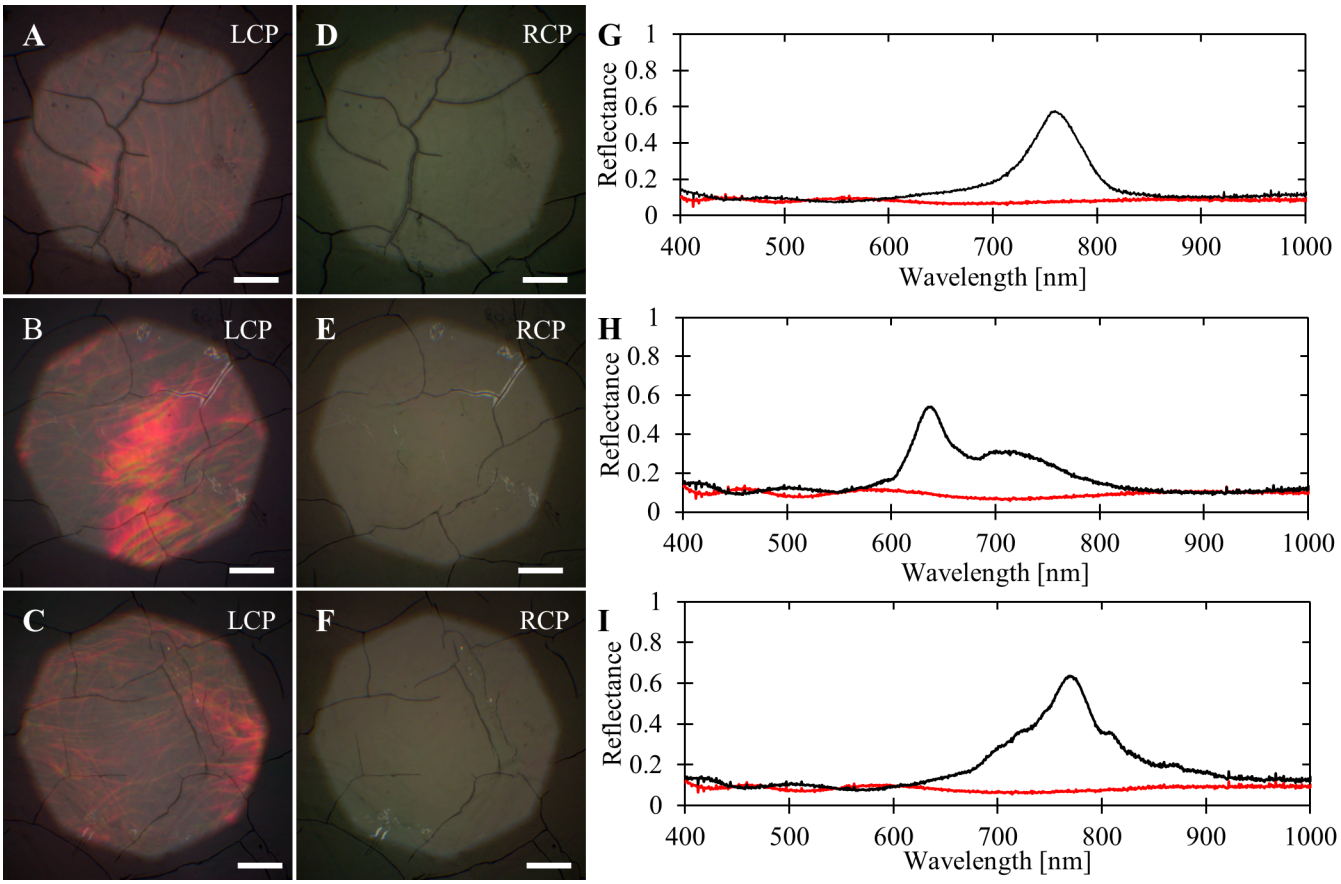

Figure S13. Polarized optical microscopy of s-ChNC films after alkaline treatment. Representative micrographs of s-ChNC films after alkaline treatment when viewed in reflection (**A, B, C**) collecting only left circularly polarized light (LCP), and (**D, E, F**) only right circularly polarized light (RCP). Scale bars are 1 µm. (**G, H, I**) Corresponding micro-spectroscopy for LCP light (black line, clear peak) and for RCP (red line, no peak). The baseline offset (*ca.* 0.1) originates from the reflection at the air/chitin interface.

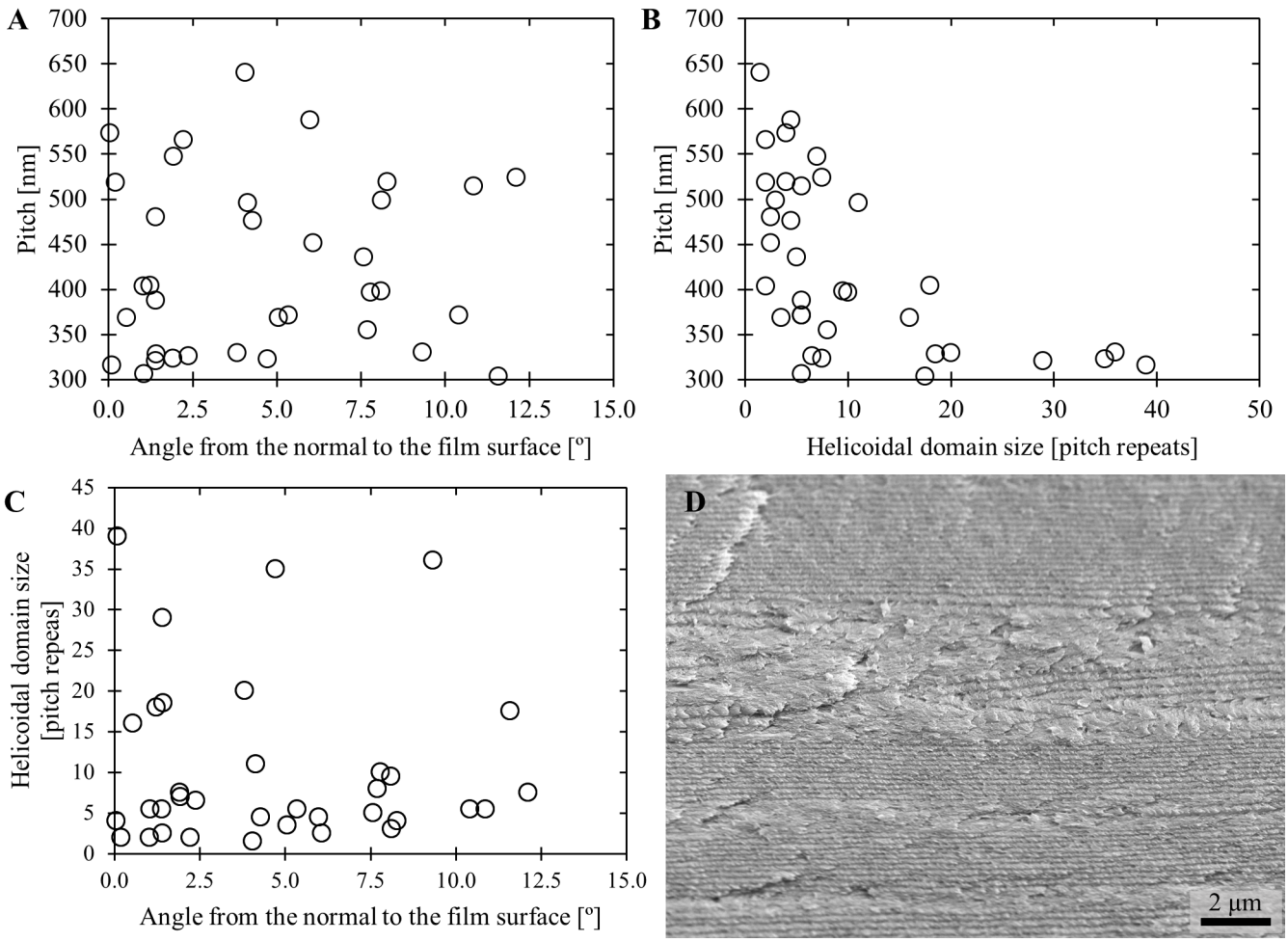

Figure S14. The pitch distributions for helicoidal domain: (**A**) Plotted against the helicoidal domain angle, as defined with respect to the line perpendicular to the film surface. (**B**) Plotted against the helicoidal domain size, as expressed in pitch repeats. (**C**) Helicoidal domain size plotted against the helicoidal domain angle. Values were measured from the cross-sectional SEM images for an f-ChNC film. (**D**) Example of a misaligned helicoidal domain seen by cross-sectional SEM image of an f-ChNC film.

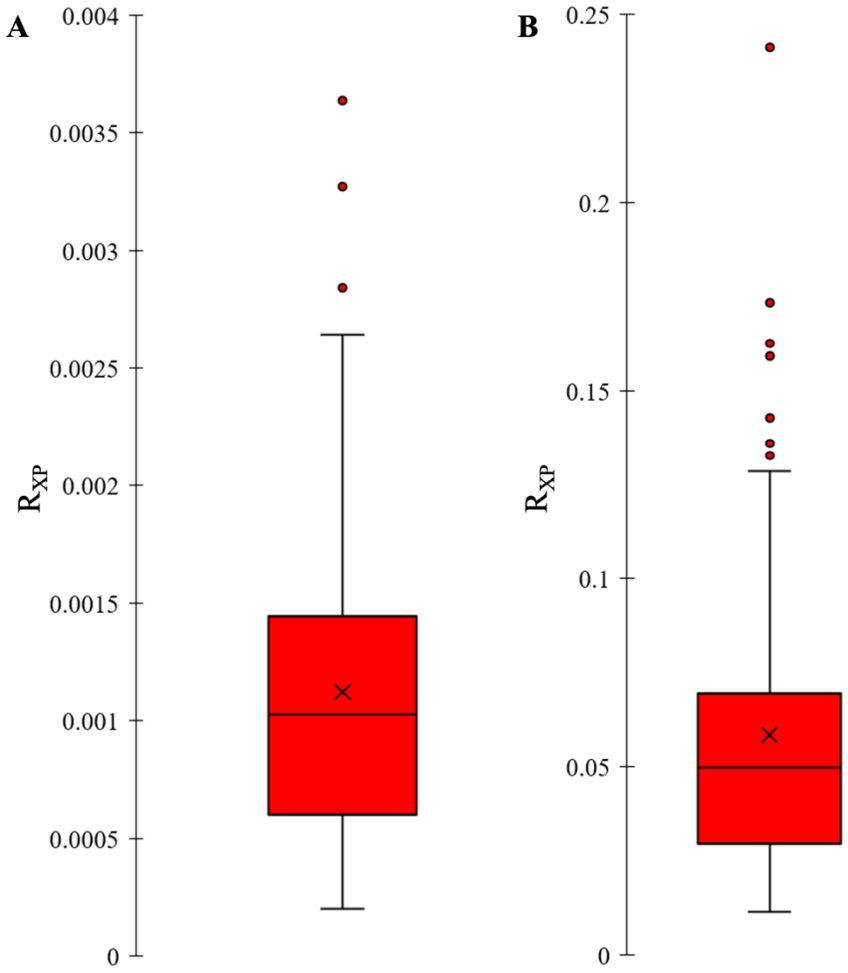

Figure S15. A statistical distribution of the maximal reflection of the peaks of a f-ChNC film (A) before and (B) after alkaline post-treatment. The "×" marks the mean value. The horizontal line marks the median line. The error bars mark the standard deviation. Circles mark the outliers. When determining maximal reflection, the background reflection was removed. The data was obtained from at least 90 individual spectra. R_{XP} denotes reflection measured between crossed polarizers.

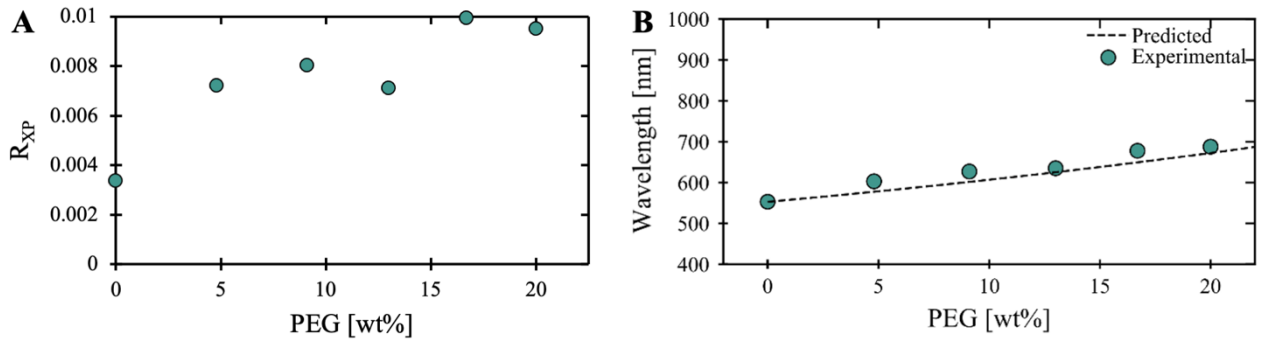

Figure S16. Effect of the addition of PEG within ChNC films, in terms of (**A**) peak reflectance and (**B**) peak wavelength from cross polarized (XP) optical micro-spectroscopy. The latter is compared to predictions for a non-volatile and chirally non-interacting additive (dotted line). Poly(ethylene glycol) red-shifts the reflected color, which is consistent with previous observations on structurally colored cellulose nanocrystal films.[3]

References

[1] H. D. Vries, *Acta Crystallogr.* **1951**, *4*, 219.
[2] C. Honorato-Rios, A. Kuhnhold, J. R. Bruckner, R. Dannert, T. Schilling, J. P. F. Lagerwall, *Front. Mater.* **2016**, *3*, 21.
[3] K. Yao, Q. Meng, V. Bulone, Q. Zhou, *Adv. Mater.* **2017**, *29*, 1701323.